How Do Discrete Global Grid Systems Actually Perform? A Systematic Benchmark Across Geometry, Computation and Relational Joins

LEVENTE JUHÁSZ, Geospatial Analytics, Technology and Open Research (GATOR) Laboratory, School of Forest, Fisheries and Geomatics Sciences University of Florida, USA

As geospatial datasets exceed the billion-row threshold, Discrete Global Grid Systems (DGGS) promise to replace expensive vector spatial joins with fast relational hash-joins on discrete cell identifiers. However, the real-world performance of different grid implementations and the upfront cost of converting vector geometries into grid indexes remains largely unquantified. This paper introduces `dggs-bench`, an open-source benchmarking framework that standardizes spatial operations across disparate grid libraries, and demonstrates it by evaluating four DGGS (H3, S2, rHEALPix, ISEA4H) and two legacy planar grids (XYZ Tiles, Geohash) across geometric fidelity, topological resilience, computational throughput, and relational performance experiments. Pre-computed DGGS equi-joins universally outperform `ST_Intersects` baselines by 13×–457×, with all grids completing ten-million-point joins in under 200 ms on a consumer workstation. On-the-fly polygon covering is not competitive at macro scales for any grid, though break-even query thresholds drop dramatically at coarser resolutions while maintaining $\geq$ 99% spatial accuracy. ISEA4H achieves competitive join performance and strict equal-area compliance but incurs covering costs up to 154× higher than H3, exposing a tooling maturity gap rather than a geometric limitation. Across all experiments, computational performance rank runs in partial reverse of geometric correctness. The benchmarking framework and all experimental data are openly available [23, 25].

CCS Concepts: • **Applied computing** → **Earth and atmospheric sciences**; • **Information systems** → **Geographic information systems**; Location based services; *Information retrieval query processing*.

Additional Key Words and Phrases: Discrete Global Grid Systems, DGGS, Spatial Join, DuckDB, Relational Database, benchmark

ACM Reference Format:
Levente Juhász. 2026. How Do Discrete Global Grid Systems Actually Perform? A Systematic Benchmark Across Geometry, Computation and Relational Joins. 1, 1 (May 2026), 39 pages. https://doi.org/XXXXXXX.XXXXXXX

Author's Contact Information: Levente Juhász, levente.juhasz@ufl.edu, Geospatial Analytics, Technology and Open Research (GATOR) Laboratory, School of Forest, Fisheries and Geomatics Sciences and University of Florida, Ft. Lauderdale, Florida, USA.

ACM XXXX-XXXX/2026/5-ART
https://doi.org/XXXXXXX.XXXXXXX

1 Introduction and Motivation

There is a long-standing claim that 80% of information is geospatially referenced. While scientific re-evaluation and empirical analysis of domain-neutral corpora suggest a more conservative estimate of 60% of information carrying direct or indirect geospatial context [20], it is now universally accepted that the volume and velocity of modern geospatial data have fundamentally outpaced the foundational architectures of Geographic Information Systems (GIS). This is codified in massive, high-resolution global datasets such as the Overture Maps Foundation, which contains over 4.2 features across themes [26], almost 3 billion global building footprints from sources like Google and Microsoft [36] or the Global Biodiversity Information Facility (GBIF) over 3 billion georeferenced occurence records [3], to name a few. Earth Observation and Digital Earth platforms also routinely generate petabytes of high-throughput data [4]. However, the underlying data models connecting this information remain largely anchored in legacy continuous coordinate systems (floating-point latitude and longitude) and local 2D planar map projections [17]. This reliance on vector geometry and traditional R-Tree based indexing method incurs a severe computational penalty: determining spatial relationships (e.g., point-in-polygon assignment) requires complex, floating-point math that scales poorly across billions of records and in areas with dense overlap [31, 38]. Furthermore, forcing spherical planetary data onto flat coordinate planes inevitably introduces severe limitations dubbed the "planar fallacy" [24], where mathematical operations executed on projected coordinates generate hidden geometric distortions affecting area, shape, and topological relationship. As researchers increasingly turn to GeoAI and global-scale modeling, architectures constrained by floating-point vector math become the primary bottleneck computational and the planar artifacts may hinder analytical performance and scientific validity.

Discrete Global Grid Systems (DGGS) have emerged as the primary structural solution to these bottlenecks. By tessellating the globe into a hierarchical, spherical index, DGGS convert complex geographic shapes into sets of discrete, scalar cell identifiers [2, 44]. This paradigm shift transitions spatial operations away from floating-point geometry and toward optimized, relational database joins on integer arrays or character strings. However, while the theoretical properties and geometric distortions of competing grid schemas are well-documented in the literature [27, 28], their practical, computational implementations have only been explored sporadically [5] and remain largely opaque. Developers and scientists adapting DGGS systems face a fragmented ecosystem of varying architectures (native compiled code vs. pure Python implementations) and grid topologies (triangles, squares, pentagons, hexagons). This structural fragmentation presents a critical challenge: choosing the "correct" grid implies adopting entirely different tessellation artifacts and underlying software architectures. As laid out in the research agenda addressing the planar fallacy [24], there is currently no independent, systematic evaluation comparing the real-world scalability, system throughput, and the the upfront computational cost of converting vector geometries to discrete grids across these modern DGGS libraries.

1.1 Contributions of this Study and Paper Organization

To fill this gap, this paper introduces `dggs-bench`, an open-source, extensible benchmarking framework designed to evaluate the operational viability of DGGS implementations against traditional vector spatial index baselines. We demonstrate the capabilities of `dggs-bench` by providing the first end-to-end empirical analysis of both geometric fidelity and raw execution throughput. The experiments executed by the framework utilize uniform Fibonacci spherical lattices as the primary sampling metrhodology to conduct unbiased stability evaluations across the globe, complemented with a 10-million-point sample of the FourSquare Open Source Places dataset to stress-test relational throughput across complex real-world point distributions. Specifically, the main contributions of this paper are:

- **Extensible Benchmarking Framework:** We introduce `dggs-bench`, a hardware-agnostic, open-source benchmarking utility featuring a modular interface that standardizes spatial operations. This allows researchers to seamlessly plug in new DGGS libraries and construct custom geometric or throughput experiments uniformly.
- **Benchmark Commonly Used Grids:** We illustrate the capabilities of `dggs-bench` by providing a comprehensive evaluation of four DGGS (H3, S2, rHEALPix, ISEA4H) and two legacy grids (XYZ Tiles, Geohash) across four experiments:
  - **Geometric Fidelity:** We quantify mapping distortions present in grids across area, direction and compactness using $1,000,000$ global, uniformly distributed sampling locations.
  - **Topological Resilience:** We model boundary seamlessness and adjacency failure rates across extreme geographic singularities (the Poles and the Antimeridian),
  - **Computational Throughput Analysis:** We profile the per-operation latency of core DGGS primitives — point encoding, polygon decoding, k-ring traversal, and hierarchical aggregation — across six grid systems on a controlled reference platform, isolating implementation-level algorithmic efficiency from data volume and I/O effects.
  - **Relational Throughput Metrics:** Using $10,000,000$ sample points from FourSquare Open Source POIs dataset to replicate typical real-world point distributions, we evaluate spatial capture accuracy and map the exponential ETL cost of using DGGS. By varying boundary generalization (1:50m vs 1:10m scales), we demonstrate the computational manifestation of increasing scale on grid indexing. These are also evaluated against traditional vector spatial joins (`ST_Intersects`).

The remainder of this paper is structured as follows. Section 2 reviews the theoretical foundations of DGGS and the current fragmentation of the ecosystem. Section 3 details the architecture of the `dggs-bench` framework. Section 4 presents empirical results of our geometric and computational evaluations. Section 5 discusses the implications of our findings and finally, Section 6 concludes the work.

2 Background and Related Work

2.1 Discrete Global Grid Systems in GIScience

The architectural limitations of treating the globe as a 2D Euclidean plane was recognized over three decades ago along with identifying the mathematical necessity of spherical-native analysis as a prerequisite for rigorous global research [41]. Following early efforts to find efficient ways to subdivide the sphere for global modeling, the foundational theory of mapping the Earth using discrete, hierarchical structures was established and formalized [27, 44]. Rather than treating geographic space as a continuous Euclidean plane, a Discrete Global Grid System (DGGS) tessellates the surface of the globe into a uniform, multi-resolution hierarchy of cells. At its core, constructing a DGGS involves a deliberate sequence of geometric design choices. The process begins with selecting a base polyhedron (typically a Platonic solid such as an icosahedron or a cube) which acts as the foundational structural wireframe. This solid is then mathematically projected onto the surface of the Earth. Once the base faces are mapped to the sphere, a recursive tessellation strategy is applied to subdivide each face into smaller constituent cells (e.g., hexagons, quadrilaterals, or triangles). The rate at which parent cells subdivide into child cells is governed by the system's aperture (refinement ratio) [44].

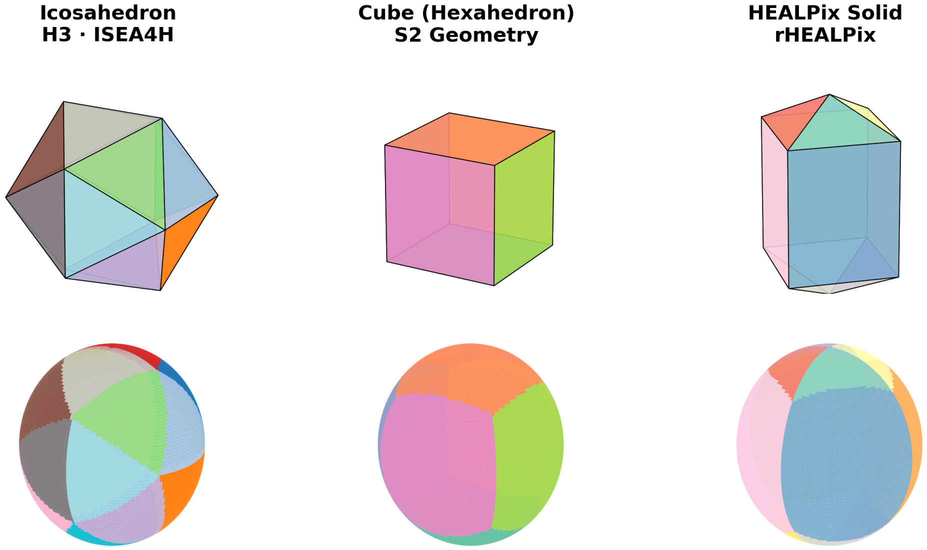

Fig. 1. The structural foundations of DGGS topologies. **Top Row:** The 3D base polyhedra serving as the initial spatial wireframe. **Bottom Row:** The spherical projection of the solid's faces onto the globe, establishing the root tessellation bounds before recursive multiresolution cell division occurs.

Figure 1 illustrates this core methodology across three prominent architectures. Uber's H3 [7] and the academic ISEA4H project an icosahedron onto the sphere, resulting in a grid mapping environment largely composed of hexagons. Google's S2 [48] utilizes a cube inscribed within the sphere, dividing its six faces into hierarchical quadrilaterals specifically to leverage space-filling Hilbert curves for rapid 1D proximity searches. Alternative schemas, such as rHEALPix [13], drop strict Platonic solids in favor of custom hybrid geometries (the HEALPix solid) tailored to preserve mathematically strict equal-area properties.

Recognizing the potential of this indexing method for heterogeneous data integration, the Open Geospatial Consortium (OGC) formalized the DGGS spatial data model in 2021 through the ISO 19170-1:2021 standard [22]. While the OGC standardization effort shows promise, the modern DGGS ecosystem remains heavily fragmented by these underlying design priorities. Because each corporate or academic implementation favors different solid orientations, projection formulas, and cell shapes, there is no spatial interoperability between them. As illustrated in Figure 2, these architectural decisions ultimately manifest as disparate visual and structural boundaries when attempting to enclose the exact same geographic region. Furthermore, Figure 2 also includes traditional hierarchical grids—specifically, Web Mercator XYZ Tiles [34] and Geohash [35]. While common in the modern GIS ecosystem, neither XYZ nor Geohash qualify architecturally as true DGGS. Operating as planar/coordinate projection grids rather than native spherical tessellations, they introduce unmitigated geometric distortion at high latitudes, contrasting the stable, bounded topologies of their true spherical DGGS.

As the field moves towards planetary-scale GeoAI models [30], this reliance on projected planar grids (termed the "Planar Fallacy" [24]) emerges as a critical structural limitation. This fallacy represents legacy of 2D cartographic abstractions. Goodchild [17] argues strongly that modern GIS

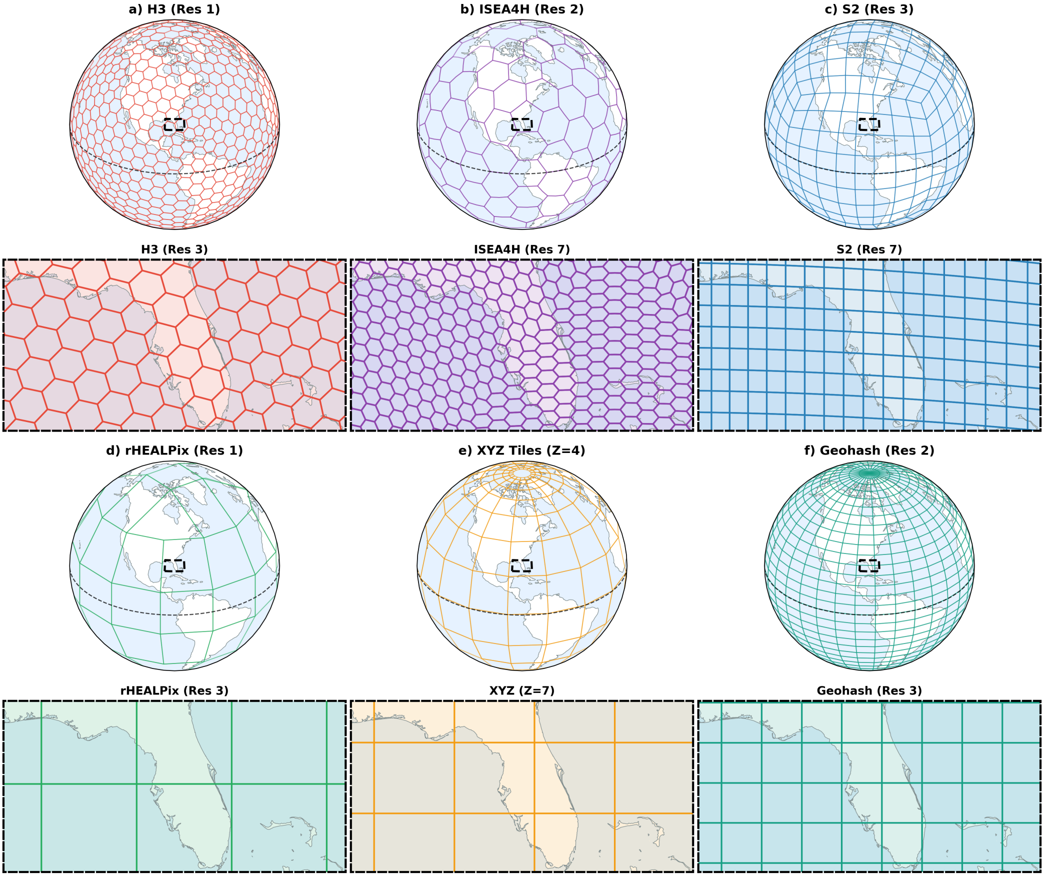

Fig. 2. The structural fragmentation of DGGS. **Top Row:** DGGS cells covering the global (generated via dggs-bench). (a) H3 hexagons developed by Uber, (b) ISEA4H equal area hexagons, (c) S2 Hilbert Quadrilaterals developed by Google, and (c) rHEALPix as an equal-area academic grid. Planar grids alternative are also shown in (e) (XYZ Tiles) and (f) (Geohash). **Bottom Row:** Localized Flat Maps (Plate Carrée) targeted over the identical sub-region showing disparate tessellation wrappers diverging structurally to enclose granular geometries.

remains "limited by the legacy of decisions that no longer make sense," particularly the continued dominance of the map metaphor over the digital globe. Reconciling these 1960s-era design choices is now essential for scaling computational performance and analytical accuracy at the global level. The emergence of planetary-scale geospatial foundation models including weather prediction systems [45] and Earth observation models like AlphaEarth [8] further motivates the need for a globally consistent, resolution-agnostic spatial index as a data infrastructure primitive. For example, early empirical evidence suggests that transitioning from planar to spherical-native architectures results can in a a 28% improvement in mapping accuracy [49], which necessitates a greater understanding of DGGS performance.

2.2 Spatial Indexing and the Vector Bottleneck

Apart the planar fallacy, the drive to adopt DGGS architectures is also motivated by the growing computational bottlenecks inherent to traditional GIS. Modern Digital Earth workloads and GeoAI pipelines [4] frequently require intersecting massive, irregular geometries (e.g. millions of Points of Interest (POIs)) against high-resolution polygons (urban areas, inundation, etc.). Historically, the geospatial community has relied on spatial index structures like R-Trees to bound and accelerate these operations [19]. While effective at a moderate scale, R-Tree implementations suffer from severe performance degradation when processing billions of records, particularly in scenarios characterized by dense geometrical overlap or highly complex polygon boundaries [31, 38].

The fundamental limitation of R-Tree-based indexing in modern high-throughput environments is its reliance on branching geometric predicates. Evaluating a point-in-polygon assignment (e.g., `ST_Intersects`) ultimately falls back to the foundational ray-casting point-in-polygon algorithm [46], and its modern, robust implementation in industry-standard libraries like GEOS (Geometry Engine, Open Source) [11]. These implementations (which serve as the computational core for PostGIS, Shapely, QGIS and many commonly used geospatial software), are characterized by data-dependent conditional evaluation and floating-point arithmetic per vertex, which prevents effective vectorization on modern CPUs and scales linearly with polygon complexity. Furthermore, because GEOS is architecturally rooted in 2D Cartesian logic, it introduces a significant 'computational tax' when forced to reconcile global spherical geometries, exacerbating the vector bottleneck in planetary-scale workloads. Effectively, an architectural transition to DGGS represents a shift from vertex-dependent geometric predicates, where intersection complexity is defined by $O(V \log N)$ relative to vertex count V and index size N, to algebraic hash-joins with an idealized complexity of $O(N)$, essentially decoupling query performance from the complexity and resolution of the original vector data.

In contrast, DGGS facilitates a transition from Geometric Topology to Algebraic Set Operations. The fundamental power of a DGGS lies not in its grid geometry, but in the simplified spatio-temporal identifiers that reduce multi-dimensional spatial analytic operations to sets of high-speed 1D array and filter operations [14]. This shift allows geospatial workloads to directly exploit the fast, vectorized query execution engines of modern analytical databases like DuckDB [40]. While the representation of DGGS indices ranges from hierarchical string literals in systems like rHEALPix [13] to bit-packed 64-bit integers in production-scale implementations like H3 [7] and S2 [48], the architectural shift toward numerical indexing is transformative for analytical throughput. When addresses are mapped to primitive integer types, spatial relationships can be resolved through bitwise operations and SIMD (Single Instruction, Multiple Data) lanes, entirely bypassing the branching overhead of the R-Tree vector bottleneck. This allows spatial join performance to scale linearly with the number of observations, independent of the original boundary's complexity [51]. While string-based representations facilitate human-readable hierarchies, they introduce a slight lexicographical 'computational tax' during prefix matching and hash-join operations in modern vectorized engines. This algebraic GIS approach ultimately aligns spatial analysis with the standard high-performance data stack, treating the globe as a continuous, indexed array rather than a collection of disparate geometric fragments.

2.3 Prior Benchmarking Efforts

The evaluation of DGGS has evolved from foundational qualitative frameworks to rigorous empirical assessments. Initial research was characterized by the establishment of "ideal" design criteria, most notably through Goodchild's early vision for hierarchical spatial structures [16] and the subsequent formalization by Kimerling et al. [27], who proposed a set of geometric and topological requirements for DGGS. These criteria, further refined by Sahr et al. [44], prioritized mathematical properties such as cell congruence, uniform adjacency, and area preservation as the primary benchmarks for "geodetic" grid validity. Recent reviews have systematically mapped the mathematical foundations and architectural configurations of prominent implementations like H3, S2, and rHEALPix. For example, one study evaluated library performance by measuring the latency of coordinate-to-cell address conversion for point samples reaching 10^6 features [5]. Another paper extended this to topographic geomorphometry, investigating how grid resolution affects the computation of slope, aspect, and curvature in hexagonal environments [29]. A rigorous baseline for geometric benchmarking, quantifying the area and shape distortion across various grid types was also established in [28]. These metrics can also be extended to the domain of deep learning, where one study identified metrics used in characterizing DGGS directly influence the performance of Spherical Convolutional Neural Networks (SCNNs) [12].

The primary challenge in integrating DGGS within cloud computing frameworks has been identified as grid encoding efficiency for big earth observation data [50]. Beyond surface-level efficiency, conventional Cartesian "flat" grid datacubes are restricted global solutions due to their reliance on localized map projections [39]. They propose that a DGGS-based topological structure facilitates a transition to array set theory, which removes the necessity for repeated, complex spatial analytic operations when fusing heterogeneous raster and vector data. This structural shift allows algorithms to be deployed globally without the computational overhead of map projection transformations. These architectural advantages are being extended through three-dimensional stratified models like ISEA4H-ESSG, which demonstrate retrieval efficiencies 20% higher than the H3 grid [32]. Despite these advancements, a significant gap remains in quantifying the operational scalability of DGGS architectures for high-throughput analytical workloads. Existing benchmarks often focus on point-level ingestion or mathematical correctness, leaving the upfront Extract, Transform, and Load (ETL) cost of polygon covering unexplored. While the Integrated Discrete Environmental Analysis System (IDEAS) established that relational DGGS implementations can outperform traditional vector data models for common GIS operations [42], these evaluations are often tied to specialized hardware appliances like IBM Netezza. Consequently, a hardware-agnostic evaluation of how boundary complexity impacts system throughput is currently missing. Furthermore, the downstream performance gains of replacing vector geometries with DGGS hashes within modern vectorized engines, such as DuckDB, remain empirically unquantified at scale. We develop `dggs-bench` to directly address these gaps, providing framework that jointly quantifies geometric fidelity, ETL overhead, and hash-join throughput across six DGGS implementations under a unified experimental protocol. Section 3 describes this software.

3 The dggs-bench Evaluation Framework

The primary objective of `dggs-bench`[1] [23] is to provide a reproducible, extensible benchmarking framework capable of evaluating diverse DGGS under identical topological and computational constraints. As illustrated in Figure 3, the framework replaces monolithic, single-use scripting in favor of a decoupled execution pipeline managed by a centralized orchestrator. To ensure reproducibility and systemic stability, the Orchestrator provides strict dependency isolation. Testing varied grid systems natively requires navigating underlying C++ bindings, intersecting spatial libraries (e.g., PROJ and GDAL), and competing memory allocators. By executing experiments within a unified architectural context, `dggs-bench` insulates the core analysis tasks from lower-level memory starvation and dependency conflicts. Furthermore, the framework orchestrates an optimized I/O pipeline. To support sweeping macroscopic queries without encountering memory

---

[1] https://github.com/gatorlab-geo/dggs-bench

limits, spatial inputs and analytical outputs are flushed from memory and serialized directly into compressed, columnar disk structures (GeoParquet) or in-memory analytical datastores (DuckDB).

Ultimately, this decoupled pipeline serves as a highly customizable testbed. The architecture is explicitly designed for straightforward extensibility. New DGGS (and other grids) can be added by authoring a lightweight plugin that conforms to the universal abstraction interface (Section 3.3). By injecting custom grids, datasets, or entirely new experiments into `dggs-bench` without modifying the core framework logic, researchers can evaluate their emerging research directly again highly optimized industrial standards (e.g. H3 or S2).

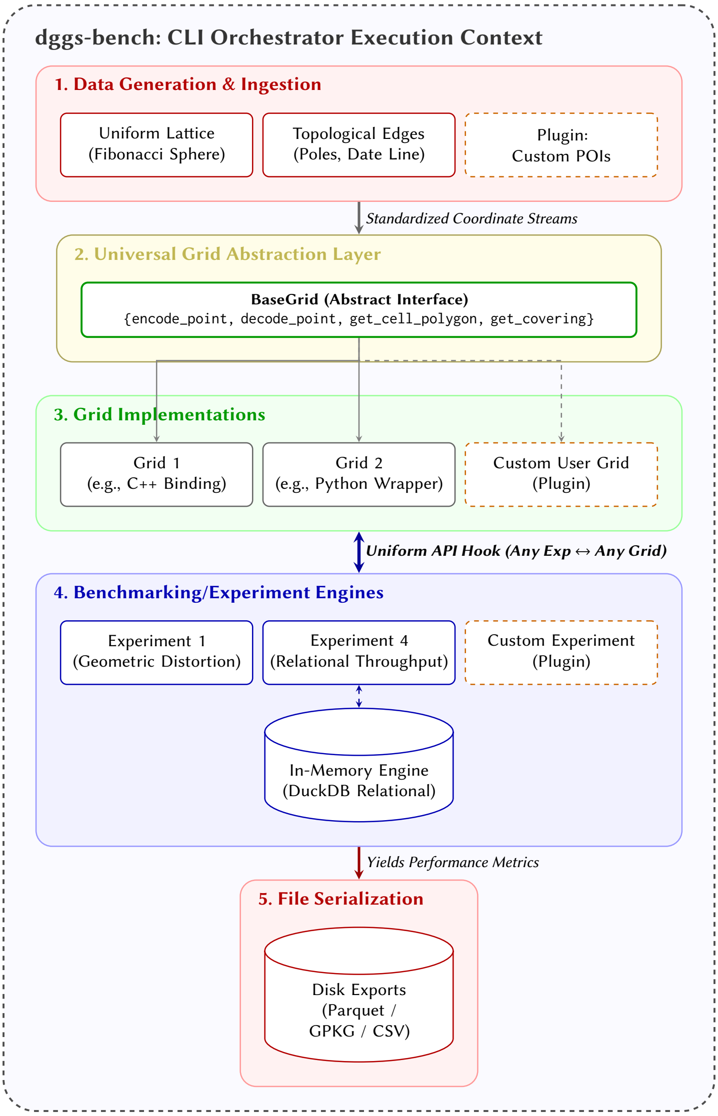

Fig. 3. The dggs-bench execution pipeline

3.1 Note on Software Development

The development of `dggs-bench` employed a human-led, AI-augmented engineering paradigm [37]. While the core system architecture, experimental methodology, and critical algorithmic logic were explicitly designed and programmed by the author, routine code synthesis and framework implementation were accelerated utilizing the AgentLoom framework [18].

This framework mitigates the well-documented hallucination and context-loss limitations of autonomous Large Language Models (LLMs) by enforcing a rule-bound governance structure that externalizes project-specific domain knowledge into a persistent knowledge graph. Building upon empirical deployments in WebGIS applications [6], an AI “Research Engineer” role was initialized and pre-loaded with DGGS theory and implementation as well as software-engineering best practices. Functioning strictly as a supervised, context-aware coding assistant rather than an autonomous developer, the agent iteratively executed localized software tasks interchangeably utilizing Claude Opus 4.6 and Google Gemini 3.1 Pro. This collaborative "human-in-the-loop" environment ensured scientific integrity while allowing the author to focus entirely on higher-order systems integration and theoretical validation. The author assumes all responsibility for the quality and validity of this software.

3.2 Data Generation and Ingestion

Naive sampling of spatial coordinates uniformly across latitude (ϕ) and longitude (λ) ranges results in a point density that increases exponentially toward the poles as physical area per grid unit shrinks, which is a direct consequence of the convergence of meridians. This oversampling introduces a structural bias toward polar geometries. To ensure that coordinate sampling remains strictly proportional to the physical surface area element dA on a sphere (formally defined as $dA = R^2 \cos\phi \, d\phi \, d\lambda$, where R is the planetary radius) `dggs-bench` generates a core synthetic lattice utilizing a Fibonacci Sphere generated via the golden spiral algorithm [15, 47]. This approach provides the distortion-free reference necessary to accurately and uniformly quantify the operational scalability of DGGS.

For a requested sample size N, the coordinates for the i-th point ($i \in \{0, 1, \ldots, N-1\}$) are deterministically calculated using the golden angle $\phi = \pi(3-\sqrt{5})$. The vertical Cartesian coordinate y_i is distributed evenly along the continuous spatial axis $[-1, 1]$:

$$y_i = 1 - \frac{2i}{N-1}$$

The dynamic radius r_i at that structural height, and the corresponding azimuthal angle θ_i, are computed as:

$$r_i = \sqrt{1 - y_i^2} \quad \text{and} \quad \theta_i = \phi \cdot i$$

These values map directly to a unit sphere (x, y, z) and are subsequently converted to geographic coordinates (EPSG:4326) via:

$$\text{Latitude}_i = \arcsin(y_i) \cdot \frac{180}{\pi}$$

$$\text{Longitude}_i = \text{arctan2}(z_i, r_i \cos(\theta_i)) \cdot \frac{180}{\pi}$$

As illustrated by the uniform distribution of the primary lattice (red) in Figure 4, this approach guarantees mathematical point uniformity. It prevents equal-area distortion metrics from artificially skewing towards polar geometric convergence. Because this underlying algorithm is deterministic, pseudo-randomization is achieved through vector-index shuffling post-generation. This randomization is important to break the spiral's inherent geographic locality, ensuring that sequentially adjacent points in the processing queue are not spatially correlated. This prevents library-level caching and memory locality effects from systematically biasing per-operation latency measurements. The seeded shuffle guarantees reproducible, identical global states across test iterations.

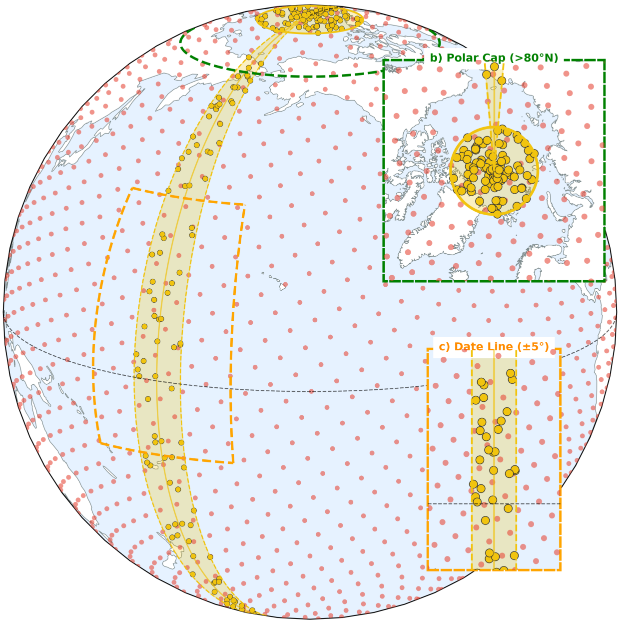

Fig. 4. A deterministic Fibonacci lattice ($N = 2000$, red) guarantees quasi-uniform topological sampling without the latitudinal clustering bias inherent to standard projections. To force boundary capability testing, explicit geographic target zones (gold) are hybridized into the arrays, specifically overloading (b) the Polar regions (> 80°N or S), and (c) the Antimeridian coordinate-wrapping seam (±5°) to rigorously evaluate planar fallacies.

3.2.1 Topological Baselines and Custom Plugin Extensibility. One of the promise of DGGS is overcoming limtations of planar grids at extremes, such as polar regions and the antimeridian where continuous coordinate geometry of planar grids fails. While the Fibonacci lattice evaluates topological uniformity, `dggs-bench` also provides a platform to stress-test grids where they may encounter critical algorithmic failures. To evaluate true boundary resilience alongside pure geometric distortion, the framework generates a secondary core dataset explicitly tracking these edge cases. The overlays in Figure 4(b, c) show explicit geographic targets (gold) that are systematically included into the pipeline to test the Antimeridian and theoretical Polar singularities.

Furthermore, adhering to the pipeline's decoupled architecture, the ingestion layer remains completely extensible. Users can bypass synthetic geometric generation entirely and plug in massive real-world datasets. This is utilized by the relational experiment engine (Section 3.4.4) and described in Section 4.5 via a 10 million sample of FourSquare Open Source POIs that is also shipped with the release of `dggs-bench`.

3.3 Universal Grid Abstraction (`BaseGrid`)

A critical challenge in standardized DGGS evaluation is systemic API fragmentation. Existing hierarchical grids are engineered to excel in different use-cases and according to disparate engineering specifications. Uber's H3 employs 64-bit integer hexagonal indexing, Google's S2 encodes cells as Hilbert curve tree-tokens, and academically-rooted grids like rHEALPix use string-based structural traversal. Without a normalization layer, a benchmark would inevitably conflate intrinsic grid geometry with library-specific design decisions.

Instead of measuring how an API was written rather than how a grid system performs, `dggs-bench` introduces the `BaseGrid` universal abstraction layer, implementing the same design pattern across all grid implementations. Its central role is to ensure grid-agnostic execution. That is, benchmarking engines invoke identical method signatures regardless of the underlying library, its programming language binding, or its internal cell representation. This strict separation ensures that experiment engines exert identical computational pressure on every grid. This makes cross-system metric comparisons scientifically meaningful by design rather than by convention. The same interface also guarantees forward extensibility: integrating a new grid system requires only subclassing `BaseGrid` and satisfying the following six structural methods, with no modifications to any experiment engine:

- `encode_point(lat, lon, res)`: Maps floating-point WGS84 coordinates to a string-cast cell identifier at a target grid resolution.
- `get_cell_polygon(cell_id)`: Reconstructs the exact topological bounding vertices of a cell as a `Shapely` Polygon.
- `get_cell_center(cell_id)`: Returns the mathematically exact geodetic centroid coordinate of the cell.
- `get_covering(polygon, res)`: Translates a complex continuous vector geometry into a discrete array of cell boundaries maximizing spatial interior coverage.
- `get_k_ring(cell_id, k)`: Retrieves topological neighbors explicitly spreading outward k discrete steps.
- `get_parent(cell_id)`: Traverses the structural hierarchy upwards to extract the topological parent.

By enforcing this contract, the benchmark orchestrator executes its scale sweeps blindly without depending on specific grid dependencies. Listing 1 shows an abbreviated implementation wrapping H3's `h3-py` Python implementation.

```python
from .base import BaseGrid
import h3
from shapely.geometry import Polygon

class H3Grid(BaseGrid):
    @property
    def name(self) -> str:
        return "H3 (Uber)"

    @property
    def is_equal_area(self) -> bool:
        return False

    def encode_point(self, lat: float, lon: float, resolution: int) -> str:
        # We exclusively cast natively to 'str' to enforce API consistency
        # across all architectures, regardless of backend typing.
        return str(h3.latlng_to_cell(lat, lon, resolution))
```

```

    def get_cell_polygon(self, cell_id: str) -> Polygon:
        # H3 expects integer or valid hex string; we pass it back
        boundary = h3.cell_to_boundary(cell_id)
        # Shapely requires closed polygons (first vertex == last vertex)
        boundary_closed = tuple(boundary) + (boundary[0],)
        # H3 returns (lat, lon), Shapely expects (lon, lat)
        lon_lat_boundary = [(pt[1], pt[0]) for pt in boundary_closed]
        return Polygon(lon_lat_boundary)
```

Listing 1. An abbreviated implementation of `BaseGrid` wrapping the `h3-py` library. This standardized contract completely isolates the complex underlying C integrations from the high-level benchmarking orchestrator.

3.3.1 Native Implementations, Interoperability, and the C++ Bridge. To formalize this abstraction layer and establish standard reference benchmarks, `dggs-bench` ships with a suite of pre-configured grids. This evaluation pipeline focuses on establishing a full geometric spectrum, utilizing six distinct grid configurations that manifest wildly divergent topologies (as previously illustrated in Figure 2). The core suite includes technology industry-standard polyhedral grids (H3, S2), academic equal-area frameworks (rHEALPix, ISEA4H), and traditional planar hierarchical mappings (Web Mercator XYZ, Geohash) to establish what these implementations can handle.

Furthermore, the abstraction layer supports cross-language interoperability via compiled bridges. For example, to evaluate the `ISEA4H` grid without experiencing pure-Python latency bottlenecks, we integrated `DGGRID`'s [43] internal `dglib` C++ spatial library directly into the system. This choice is partly motivated by recent advancements in the `DGGRID` engine, such as the mathematical modeling of multi-structural elements, including cell centers, vertices, and edges, to enhance precision for both raster and vector data processing [21]. By leveraging `pybind11`, the C++ coordinate encoders and boundary serializers were wrapped as a localized module and subclassed gracefully under `BaseGrid`. Our bridge effectively makes these native C++ enhancements accessible to the Python-based spatial data science ecosystem. The benchmarking engines described below remain fundamentally "blind" to whether they are invoking a pure-Python Hilbert curve generator (S2) or a statically optimized C++ coordinate transformation (ISEA4H). This eliminates framework bias and proves the viability of the repository as an industrial spatial testbed.

A guiding principle of the `dggs-bench` pre-configured suite is that each grid is wrapped via the best publicly available binding at the time of evaluation. We define this as the implementation that is most actively maintained, most widely adopted by practitioners, and most stable for production use. This criterion deliberately takes precedence over strict architectural comparability. Because `dggs-bench` is intended to reflect the real-world state of the DGGS ecosystem rather than a controlled laboratory idealization, a grid's accessible performance ceiling is more informative than its theoretical maximum. Where a compiled binding is unstable or unavailable, the framework favors the most performant stable alternative. Examples of this principle in practice are the selection of `s2sphere` over the SWIG-bound `s2geometry` and the development of a custom `pybind11` bridge for ISEA4H (See Section 4.1). These choices ensure that performance results carry a clear provenance: they reflect what a developer or researcher would obtain today.

3.4 Benchmarking Engines

Because spatial constraints can vary depending on the application area, `dggs-bench` avoids monolithic execution logic. Instead, benchmarking operations designed for this paper are decoupled into four modular "Engines" designed to accept an instantiated `BaseGrid` and a target geospatial array without modification.

3.4.1 Geometric Fidelity Engine.

Designed to establish a strict mathematical baseline, the Geometric Fidelity engine quantifies the intrinsic structural distortion of the chosen topological grids. It iteratively evaluates uniform Fibonacci arrays, reconstructing the corresponding DGGS cell's native `shapely` boundaries using exact geodetic mathematics rather than planar Euclidean approximations. The engine explicitly measures three primary geometric dimensions:

1. **Geodetic Area:** The engine computes the absolute physical area natively wrapped on the WGS84 ellipsoid. This exposes the exact statistical variance of cell capacity.
2. **Zone Standardized Compactness (ZSC):** Proposed by Kimerling et al. [27] specifically for evaluating global grids, ZSC measures a cell's perimeter efficiency by dividing it by the perimeter of a theoretically perfect spherical cap of the same area. This metric identifies structural warping where polygons ”stretch” as they approach base topological projection seams.
3. **Angular Distortion:** To evaluate spatial conformality (i.e. how well a cell preserves its localized shape), the engine calculates the statistical variance of internal corner angles against their ideal planar forms (e.g., 120° for a regular hexagon). This metric exposes the physical "shearing" of the boundary edges caused by spherical coordinate mapping.

These three metrics form a comprehensive evaluation suite. By serializing this information, the benchmark can automatically map the precise geographic distribution of structural compromises required to enforce discrete tessellations around bounding planetary singularities.

3.4.2 Topological Resilience Engine.

While DGGS excel in normalized continuous space geometries and operate natively on spherical surfaces, edge-case coordinates may provoke arithmetic and positional instability originating from underlying software implementation flaws. Drawing on the specific stress-test vectors outlined in Section 3.2, the Topological Resilience engine bombards implementations precisely along the Antimeridian coordinate-wrapping seam ($\pm 180°$) and at theoretical singularities near the North and South Poles ($> 89°$), as illustrated in Figure 4.

Beyond merely tracking absolute process exceptions, geometric polygon inversions, and catastrophic spatial tracking loss, the engine actively probes the resilience of the grid's adjacency network. By executing exhaustive k-ring traversals explicitly across these fault lines, the engine audits raw neighbor counts (e.g., detecting missing, duplicated, or invalid topological adjacencies common at polar pentagons or base-cube corners) and calculates the true geodetic neighbor distances between adjacent cell centroids. Ultimately, by auditing neighborhood topologies at known singular coordinates, the engine distinguishes grid implementations that maintain consistent adjacency under true spherical topology from those whose apparent global coverage conceals planar approximation artifacts at extreme latitudes and meridional discontinuities.

3.4.3 Computational Latency Engine.

This engine quantifies the raw CPU throughput of each grid implementation across the four primitive operations that compose any DGGS analytical workflow:

- **Encode:** Translating a WGS84 coordinate pair to a cell identifier string.
- **Decode:** Reconstructing the cell boundary as a Shapely polygon.
- **K-Ring:** Retrieving the set of cells within topological distance $k = 1$ (immediate neighbors).
- **Parent:** Resolving the containing cell at the next coarser resolution level.

These four operations were selected because they represent the full suite of grid surface operations, that is, encode and decode stress the forward and inverse spherical projection, k-ring stresses horizontal topological traversal and parent stresses vertical hierarchical traversal.

However, measuring latency across evaluation sequences using massive evaluation datasets introduces a critical benchmarking hazard: generating and simultaneously holding millions of complex vector polygons in active memory will quickly exhaust available system RAM. When memory limits are repeatedly breached, the operating system invokes background memory-sweeping processes that introduce severe, unpredictable computational slowdowns. To prevent this overhead from artificially skewing the results, each operation is timed in isolation and the resulting geometry object is discarded immediately after the timing window closes. This streaming evaluation ensures that measured latency reflects the algorithmic cost of the grid operation rather than incidental OS page-swapping induced by accumulating millions of polygon objects in memory.

3.4.4 Relational Database Throughput Engine. Designed to quantify the performance of grid-indexing, this engine simulates industrial data-lake workloads by orchestrating a localized instance of DuckDB. The goal is to explicitly quantify the structural trade-off of a DGGS workflow: the initial Extract-Transform-Load (ETL) “tax“ to encode geometries versus the compounding query execution “reward.“ This engine evaluates the spatial assignment pipeline across three distinct operational phases:

1. **The ETL Phase (Points and Polygons):** The engine records the exact computational latency required to independently encode massive arrays of raw coordinate points into discrete DGGS identifiers. Simultaneously, it logs the time required to generate bounding grid arrays (”coverings“) capable of encapsulating complex map polygons. To test software library maturity, the engine natively delegates this boundary rasterization to the underlying grid’s internal polyfill algorithms whenever available.
2. **Query Execution:** With all geometry discarded and entirely discretized into primitive data types, the engine executes point-in-polygon assignments natively within the database using standard relational equi-joins on the string or integer hashes, recording the elapsed query latency.
3. **Vector Baseline Comparison:** To evaluate these metrics scientifically, the engine executes the structurally identical spatial operation, utilizing the original floating-point vector geometries driving DuckDB’s native `spatial` extension (`ST_Intersects`).

By executing this evaluation, the benchmark captures two concurrent metrics. First, it derives absolute DGGS *spatial capture accuracy* by dividing the total number of matched points returned by the relational index join against the ground-truth intersection count formally extracted by the vector baseline. Second, comparing the two recorded execution times objectively reveals the magnitude of downstream query speedup achieved when complex spatial mathematics are replaced by indexed database keys.

3.5 Data Serialization and Provenance

To ensure reproducibility and structural transparency, `dggs-bench` decouples its computational benchmarking engines from visual analysis. The framework purposefully avoids generating plots, synthetic summaries, or destructive data aggregations within the active execution loops. Instead, all engines are constrained to strictly output raw, unaltered runtime metrics and geometric payloads to stable disk storage. The framework natively serializes massive multi-million row evaluation matrices (e.g. topological neighbors extracted from one million coordinate array) directly out of volatile memory and into columnar Parquet files. This guarantees that payloads compress efficiently while optimizing localized data-read throughput speeds for subsequent analysis.

Furthermore, to ensure strict interoperability with the broader Free and Open Source Software for Geospatial (FOSS4G) community, the serialization layer retains the ability to export georeferenced output directly into the Open Geospatial Consortium (OGC) standard GeoPackage format (`.gpkg`) and standard `.csv` sheets.

4 Experimental Results

4.1 Experimental Setup and Grids

To validate the `dggs-bench` abstraction layer across varying programmatic environments, we selected six spatial index implementations spanning the full architectural spectrum of modern geospatial indexing. Rather than treating these implementations as interchangeable, we organize them into three tiers reflecting their underlying design priorities, as shown below. The grids and their underlying dependencies are summarized in Table 1, and their visual representation is shown in Figure 2.

Across all tiers, the library selected for each grid represents the best publicly available, actively maintained implementation as of the time of writing (i.e. the tool we assume a developer or researcher adopting that grid would realistically use today). For example, both a pure-Python port (`s2sphere`) and a SWIG binding exists `s2geometry` for S2. However, the theoretically more performant `s2geometry` is designated as "unstable" by the maintainer, Google. For this reason, `s2sphere` as the most stable option was selected. This criterion of practical accessibility is a deliberate methodological choice. While the selected implementations are architecturally heterogeneous, together they constitute an accurate representation of the current state of the DGGS ecosystem. The performance gaps documented in Sections 4.3–4.5 are therefore not merely implementation artifacts but a true characterization of what is operationally achievable with each grid for a developer or researcher today.

- **Tier 1 - Industry DGGS ($T1$):** Production-grade spherical tessellations backed by major technology companies, designed for large-scale deployment. H3 [7] is accessed via `h3-py`, whose Cython-compiled C-core eliminates Python interpreter overhead entirely. S2 (Google) [48] is accessed via `s2sphere`, a pure-Python port of the C++ library, selected over the SWIG binding (`s2geometry`) [2]
- **Tier 2 - Academic DGGS ($T2$):** Spherical tessellations originating from the research community, prioritizing strict mathematical properties — equal-area preservation and topological correctness — over deployment convenience. rHEALPix [13] is accessed via the `rhealpixdggs` pure-Python library. ISEA4H [9, 44] uses a custom `pybind11` bridge to the `dglib` C++ library developed as part of this work, since no production Python binding exists. These grids represent the current state of the art in the academic DGGS ecosystem.
- **Tier 3 - Legacy Planar Baselines ($T3$):** Planar hierarchical indexing schemes that are neither spherical nor equal-area, but remain prevalent in production GIS deployments. Geohash [35] is accessed via `polygon-geohasher` and `python-geohash`. Web Mercator XYZ Tiles [34] via Mapbox's `mercantile` library. These are included as representative incumbents against which DGGS performance gains are contextualized.

All test suites were orchestrated through the `dggs-bench` framework under Python 3.12 and executed on a consumer workstation (AMD Ryzen AI 9 HX PRO 370, 12 cores / 24 threads; 64 GB DDR5 RAM; 1 TB NVMe SSD) running Ubuntu 24.04 LTS, to simulate democratized spatial-data pipelines accessible without specialized hardware. Core geospatial computations used `Shapely` 2.1.2 over GEOS 3.13.1. Grid libraries were pinned to H3 v4.4.2, s2sphere 0.2.5, and PROJ 9.7.1. Relational join benchmarks were executed within a DuckDB 1.5.1 in-process instance to maximize vectorized string-hash matching. The ISEA4H C++ bridge was compiled with GCC 13.3. Complete experimental datasets are available at [25].

---

[2] The native SWIG-bound S2 would likely achieve H3-level performance, however at the time of writing it is still considered highly unstable by Google (see https://github.com/google/s2geometry/blob/master/README.md

Table 1. Evaluated Geospatial Indexing Frameworks and Dependencies

Grid	Library	Backend	Base Solid	Cell Shape
H3 (Uber)	`h3-py` (v3.7)	Cython (C-core)	Tilted Icosahedron	Hexagon*
S2 (Google)	`s2sphere` (v0.2.5)	Pure Python port	Spheroid Cube (Conformal)	Quadrilateral
rHEALPix	`rhealpixdggs`	Pure Python	HEALPix Equal-Area Solid	Quadrilateral
ISEA4H	`dglib` (v2.1)	pybind11 (C++)	Icosahedron (Equal-Area)	Hexagon*
Geohash	`python-geohash`, `polygon-geohasher`	C-ext + Pure Python	Equirectangular	Rectangle
XYZ Tiles	`mercantile` (v1.2.1)	Pure Python	Web Mercator (Cylinder)	Rectangle

** Tessellation includes 12 base pentagons to resolve icosahedral vertex curvature (see [44].*

4.2 Geometric Fidelity

We quantified the intrinsic geometric distortions of all six grids by distributing $N = 1,000,000$ Fibonacci-sphere-sampled geodetic evaluation points (Section 3.2). Grid resolutions were selected to align all implementations near the $\approx 1\,\text{km}^2$ cell footprint threshold, providing a common physical reference scale for comparison. For each sampled point, the corresponding cell boundary was reconstructed and three metrics were computed: normalized area, Zone-Standardized Compactness (ZSC), and angular deviation. Table 2 summarizes the results.

Table 2. Global Geometric Distortion Benchmarks ($N = 10^6$ Fibonacci-sphere sampling)

	Norm. Area			**ZSC**				**Angular Dev. (°)**		
Grid	std	min	max	mean	std	min	max	mean	std	max
H3	0.12	0.59	1.35	0.95	0.00	0.00	0.95	2.32	1.75	14.65
S2	0.15	0.59	1.24	0.88	0.01	0.76	0.89	8.87	7.80	34.82
rHEALPix	0.00	0.99	1.00	0.87	0.03	0.51	0.89	7.33	12.51	59.91
ISEA4H	0.00	1.00	1.06	0.95	0.00	0.00	0.95	6.66	2.34	33.15
Geohash	0.28	0.00	1.27	0.85	0.03	0.02	0.89	0.00	0.07	51.95
XYZ	0.44	0.01	1.49	0.89	0.00	0.89	0.89	0.01	0.01	0.03

4.2.1 Area distortion. Figure 5 (left column) shows the full latitudinal and longitudinal normalized area profiles.

Tier 1 - Industry DGGS. H3 and S2 both exhibit moderate area variance ($\sigma = 0.12$ and 0.15 respectively) originating from the distortion introduced when projecting their base polyhedra onto the sphere. H3 cells range from 0.59× to 1.35× the mean cell area, and S2 cells from 0.59× to 1.24×, with the extremes concentrated near icosahedral and cube-face projection seams, that are also visible on the ortographic heatmaps provided in Appendix Figure A1. Both grids maintain continuous global coverage.

Tier 2 - Academic DGGS. Equal-area grids (rHEALPix, ISEA4H) achieve normalized area standard deviations of 0.00, confirming strict equal-area enforcement by design. rHEALPix cells range from 0.99× to 1.00× the mean; ISEA4H from 1.00× to 1.06×. The marginal upper exceedance in ISEA4H reflects the 12 pentagonal cells at icosahedral vertices, which deviate slightly from the hexagonal mean. Their presence is not an implementation artifact but a topological necessity as Euler's polyhedron formula demands exactly 12 pentagons for any hexagonal tiling of the sphere, irrespective of resolution (See [44]).

Tier 3 — Legacy Planar Grids. Geohash and XYZ Tiles exhibit severe and systematic area distortion. XYZ cells near the equator span 1.49× the mean tile area while polar cells shrink to 0.01×, a direct consequence of the Web Mercator cylindrical projection. The truncation at ±85.05° is a direct consequence of the Mercator projection's scale factor $\sec\varphi$, which grows without bound as $\varphi \rightarrow 90°$, causing projected cell areas to diverge toward infinity at true polar coordinates. The truncation replaces this singularity with an encoding failure, meaning polar regions are simply absent rather than severely distorted.

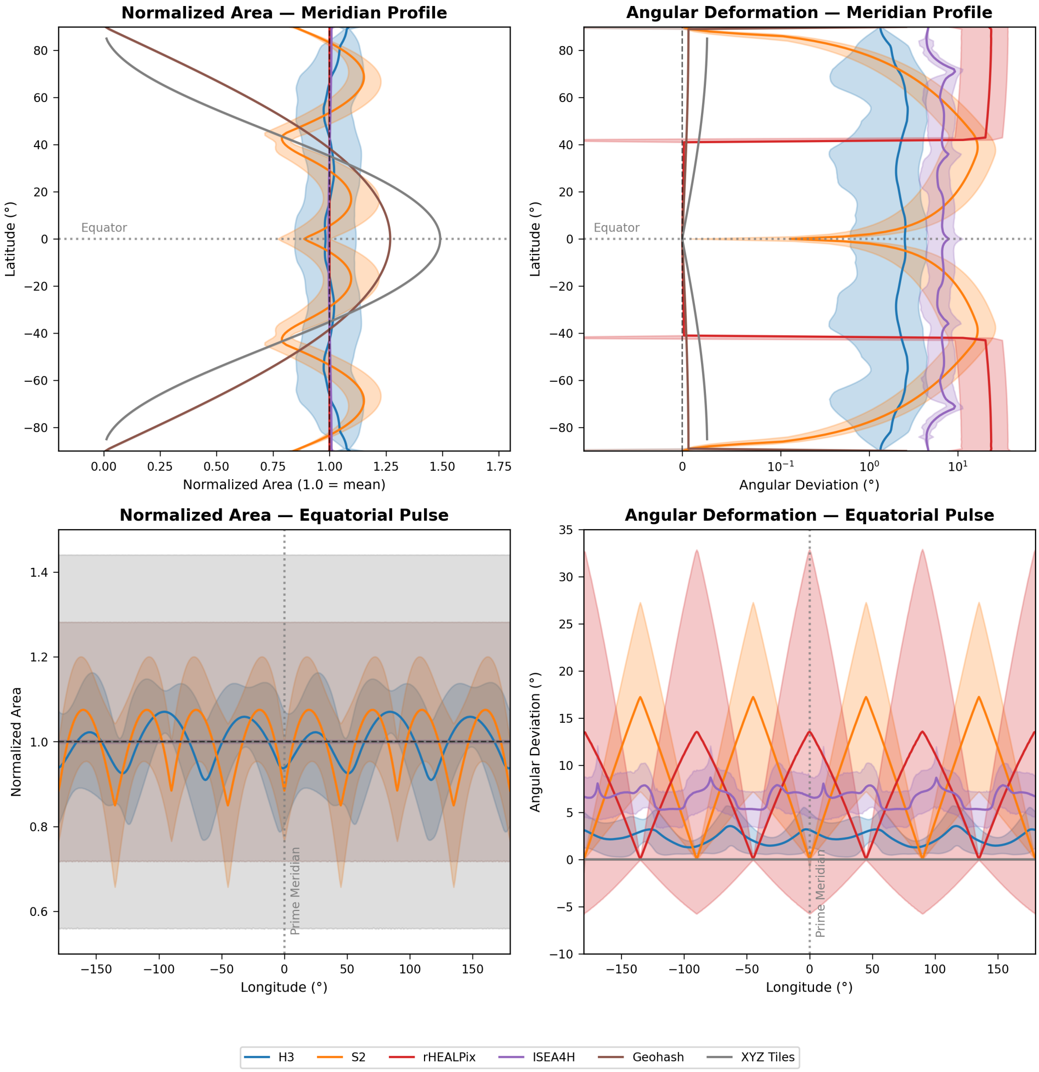

Fig. 5. Normalized area ratio (left column) and angular deviation (right column) plotted across latitude (top row) and longitude (bottom row). Tier 1 grids oscillate symmetrically around the 1.0 baseline tracing their base solids; Tier 2 grids are flat; Tier 3 grids collapse toward the poles.

4.2.2 Angular distortion. Angular distortion exposes a fundamental trade-off between area fidelity and shape conformality.

Tier 1 — Industry DGGS. H3's hexagonal topology closely approximates the isotropic boundary of a circle, which minimizes shear across projection seams. H3 achieves the lowest peak angular deviation among all native DGGS, with a mean of 2.32° and a maximum of 14.65°. S2's quadrilateral cells, which must bend 90° corners onto a sphere, exhibit greater cyclic shearing ($\mu = 8.87°$, $\sigma = 7.80°$, max = 34.82°), concentrated at cube-face boundaries.

Tier 2 — Academic DGGS. rHEALPix exhibits the most extreme shear of any native DGGS ($\mu = 7.33°$, max = 59.91°), with the peaks concentrated precisely at the ±41.81° latitudinal collars where the HEALPix projection transitions between its equatorial cylindrical and polar-cap regions. Within those equatorial bands, rHEALPix conversely achieves near-zero angular deviation — a mathematical consequence of its cylindrical equal-area construction. ISEA4H records a mean deviation of 6.66° and a maximum of 33.15°, higher than H3 due to fewer cells per icosahedral face and a different face orientation. The geographic distribution of these shear patterns is shown in Appendix Figure A2.

Tier 3 — Legacy Planar Baselines. Both Geohash and XYZ Tiles record near-zero mean angular deviation ($\approx$ 0.01°). This conformality is not a geometric achievement but a consequence of operating on a flat orthogonal plane: right-angle rectangular geometry is preserved by construction, at the direct expense of the severe area distortion documented above.

4.3 Topological Resilience and Continuity

While theoretical grid projections are mathematically continuous, the computational libraries executing them are subject to arithmetic bounds, conditional branch logic, and coordinate wrapping conventions. To probe these constraints, the Topological Resilience Engine stressed each implementation with coordinate sets concentrated at the North and South Poles (> 89° latitude) and along the Antimeridian (±180° longitude) and the Equator in addition to a global control distribution (Section 3.2). CPU execution time and neighbor spacing variation are summarized in Figure 6. Encoding survival rate, per-operation latency (μs), and neighbor centroid spacing variance (m) are also reported in Appendix Table A1.

Tier 1 — Industry DGGS. As seen in Figure 6, H3 demonstrated the most uniform behavior across all zones. Encoding latency was stable at $\approx 3.5\,\mu$s regardless of geographic position. This is confirmed by Cohen's d [10] ($d = 0.01$), indicating that geographic zone explains essentially none of the variance in encoding latency. This confirms that the icosahedral projection places no special computational boundary at the poles or Antimeridian. Neighbor centroid spacing showed a moderate difference between the Date Line (27.4 m) and polar zones (13.1 m, $d = 1.07$), but remains operationally negligible at this scale. S2 exhibited spacing compression at the geographic poles (5.4, m) relative to both equatorial (173.0, m, $d = -3.02$) and Date Line (178.5, m, $d = 1.92$) zones, which is a signature of the cube-face projection concentrating cells near each face's projection pole.

Tier 2 — Academic DGGS. rHEALPix showed the most pronounced latency variation of any surviving grid. Its internal projection switches between cylindrical and polar-cap geometry based on input latitude, introducing conditional branching absent from icosahedral systems. Encoding at the poles (203.4 μs) is 9.2× slower than at the equator (22.0 μs, $d = 2.54$, large effect). Neighbor spacing follows the inverse pattern: equatorial spacing is compact (45.0 m) while polar regions stretch to 285.9 m, though the effect size here is smaller ($d = 0.13$) due to high within-zone variance. ISEA4H survived all zones without failure and maintained consistent encoding latency ($\approx 25\,\mu$s, negligible

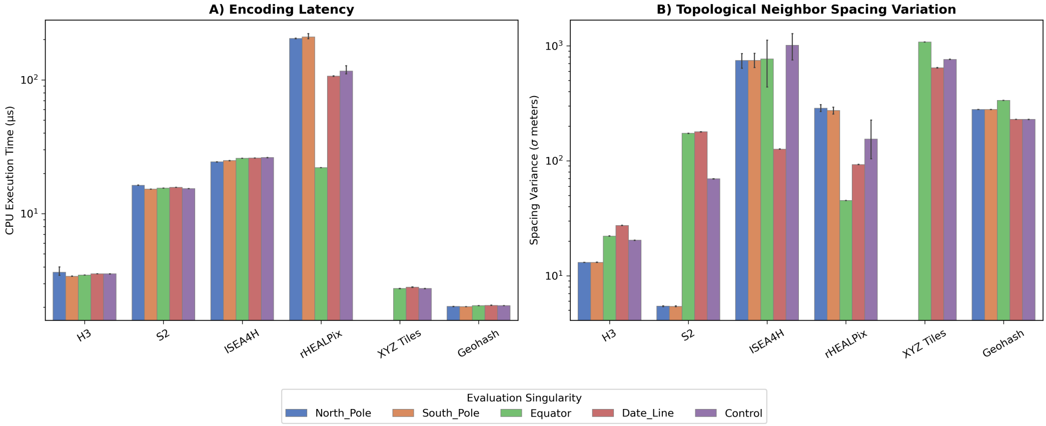

Fig. 6. Topological resilience across geographic singularities. (A) Per-operation encoding latency by zone; (B) neighbor centroid spacing variance by zone. Error bars represent 95% confidence intervals. XYZ Tiles are absent from the polar zone panels due to process-level encoding failure. Vertical scales are logarithmic.

cross-zone variation). Neighbor spacing is lower along the Antimeridian (126.2 m) compared to the global control (1,011.7 m), though Cohen's $d = -0.02$ indicates this difference in means lies within the normal variance of ISEA4H spacing. The global neighbor spacing of ISEA4H is inherently high-variance due to the uneven icosahedral face layout, making the Antimeridian suppression visible in means but not a distinct distributional shift.

Tier 3 — Legacy Planar Grids. XYZ Tiles failed entirely at both polar zones ($> 85.05°$), returning process-level encoding exceptions due to the Web Mercator projection singularity at those latitudes. Geohash, which operates directly on angular coordinate bounds without projection, survived all five zones with 100% encoding success. Its equatorial spacing (334.8 m) is moderately higher than the control (228.7 m, $d = 2.01$), reflecting the rectangular cell geometry expanding in the east-west direction near the equator.

4.4 Computational Latency

Theoretical geometric integrity is a necessary but insufficient condition for practical deployment and widespread adaptation of DGGS. Implementations must also fit within the computational requirements of large-scale geospatial data ingestion and processing pipelines. To evaluate throughput under a globally representative and reproducible point distribution, the Computational Latency experiment was executed against $N = 10^7$ coordinates generated via the Fibonacci sphere algorithm (Section 3.2), ensuring that latency measurements are not confounded by geographic clustering. Three independent iteration batches were run to expose execution variance and eliminate hardware noise.

As visualized in Figure 7 and Table 3, the results vary by grid tier, but in reverse order relative to the Section 4.1 taxonomy. That is, legacy planar grids ($T3$) achieve the highest raw throughput precisely because their arithmetic simplicity forgoes spherical accuracy, while the Academic DGGS ($T2$) carry the heaviest per-operation cost. The performance driver is backend binding depth rather than the algorithmic complexity of the grid itself. Alongside each throughput measurement, Table 3 also reports the Coefficient of Variation ($CV\% = \sigma/\mu \times 100$) across the three iteration batches, which is a scale-independent measure of relative variability that quantifies how consistently each grid performs across independent runs. All *CV* values remain below 5%, indicating that the reported throughput figures are stable regardless of implementation tier.

Tier 1 — Industry DGGS. H3 achieves 854,681 encode ops/s via Cython-compiled C-core bindings that eliminate Python interpreter overhead for icosahedral projection, followed by S2 at 222,384 ops/s. S2's `s2sphere` pure-Python port introduces overhead relative to H3, though the underlying geometry remains optimized for geospatial operations. Both grids occupy a clear middle tier: faster than academic implementations by 3–20×, and slower than Planar baselines by 1.1–1.9× on encode.

Tier 2 — Academic DGGS. rHEALPix (75,228 ops/s) and ISEA4H (42,995 ops/s) reflect the cost of Python wrappers performing full spherical projection calculations or C-ABI bridge calls per batch without ahead-of-time compilation. The encode-decode asymmetry is pronounced for both: rHEALPix decode drops to 7,913 ops/s and ISEA4H to 14,896 ops/s, a $>65\%$ reduction from their respective encode speeds. This decoding penalty is universal across all six grids — geometric object instantiation from cell identifiers reduces throughput by $>85\%$ in every case.

Tier 3 — Legacy Planar Grids. Geohash achieves 1,645,309 encode ops/s by reducing spatial encoding to a lookup-table-driven base-32 string construction with no floating-point trigonometry. XYZ Tiles follow at 953,711 ops/s via direct tile index arithmetic in Web Mercator. The throughput advantage of these grids is a direct consequence of the geometric trade-offs documented in Section 4.2: omitting spherical projection eliminates the dominant computational cost.

Parent-cell inversion. Figure 7 also reveals a consistent performance inversion in the parent-cell traversal metric, which cuts across tiers. Grids whose hierarchies are encoded as integer arithmetic dominate this operation: Geohash (21,605,340 ops/s), ISEA4H (8,616,791 ops/s), and rHEALPix (6,936,522 ops/s) all exceed H3 (4,364,007 ops/s) despite their lower encode throughput. For ISEA4H, the parent cell at resolution $r-1$ is computable via a fixed arithmetic shift on the `dglib` integer cell ID, requiring no spherical re-projection. This inversion demonstrates that vertical hierarchical traversal and horizontal spatial query are governed by entirely different implementation constraints.

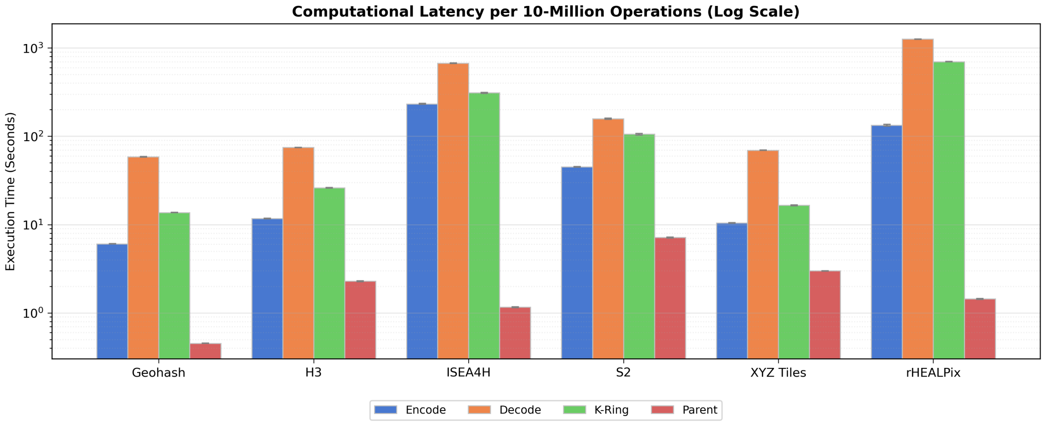

Fig. 7. Total CPU execution latency for 10^7 Fibonacci-sphere-sampled coordinates per grid, aggregated across three iteration batches (error bars: min–max range). The logarithmic scale separates the three tiers: Legacy Planar grids (Geohash, XYZ) achieve the highest throughput via arithmetic-only encoding; Industry DGGS (H3, S2) occupy the middle band via compiled bindings; Academic DGGS (rHEALPix, ISEA4H) incur the highest per-operation cost via Python wrappers.

Table 3. Computational Throughput Scaling ($N = 10^7$ Fibonacci-sphere points, three iteration batches). Variation expressed as Coefficient of Variation ($CV\%$).

	Encode		Decode		K-Ring		Parent	
Grid	**Ops/s**	**CV%**	**Ops/s**	**CV%**	**Ops/s**	**CV%**	**Ops/s**	**CV%**
H3	854,681	0.6	133,382	1.0	381,757	1.1	4,364,007	1.0
S2	222,384	0.6	63,267	1.4	94,393	1.8	1,397,123	1.3
rHEALPix	75,228	1.7	7,913	1.1	14,308	0.3	6,936,522	1.2
ISEA4H	42,995	0.9	14,896	0.8	32,249	0.8	8,616,791	1.6
Geohash	1,645,309	0.7	169,840	1.7	722,143	2.1	21,605,340	4.4
XYZ	953,711	1.2	143,122	1.4	606,985	1.0	3,281,460	3.7

4.5 Relational Throughput

To evaluate whether DGGS can replace and supersede continuous floating-point vector geometries in analytical workloads, we designed a unified multi-scale relational throughput experiment that extracts three execution stages at every hierarchical resolution level:

- *Spatial Capture Accuracy:* does cell-based grouping geometrically replicate the result of a floating-point vector point-in-polygon intersection?
- *Polygon Covering (ETL Tax):* what is the upfront computational cost of converting a vector polygon into a DGGS cell index?
- *Relational Equi-Join:* do native cell identifier joins outperform R-Tree-based `ST_Intersects` once the index is materialized?

4.5.1 Experimental Design & Vector Baselines. To stress-test implementations, we evaluated four boundary configurations that isolate different sources of computational complexity.

1. **Macro (1:50m):** Five global country boundaries (France, Brazil, South Africa, Australia, India) from Natural Earth at 1:50m generalization. Smooth boundaries with moderate vertex density.
2. **Macro (1:10m):** The identical five countries at 1:10m resolution, isolating boundary vertex density as an independent variable. This manifestation of the coastline paradox [33] directly dictates the computational complexity of geometric predicates and vector join throughput. The difference between the macro scales is illustrated in Appendix Figure A3.
3. **Macro (Europe):** 15 European countries simulating overlapping R-Tree bounding boxes to stress hierarchical spatial caching (Appendix Figure A4).
4. **Micro (Urban):** The five largest global urban extents by area from Natural Earth, representing compact geometries with high vertex density relative to enclosed area.

Following the algebraic GIS approach in [42], we simulate industrial workloads by treating spatial analysis as standard relational equi-joins on integer or string hashes. This allows us to quantify the ETL 'tax' versus the query execution 'reward' across a wider variety of grid architectures. A global dataset of $N = 10{,}000{,}000$ coordinate tuples was extracted once from the Foursquare (FSQ) Open Source Places dataset, ensuring real-world POI spatial distribution. Each boundary profile was then evaluated against this shared corpus across three independent iteration batches. Each grid was evaluated across a sweep of its native resolution hierarchy, covering a common physical cell size range from approximately 12,000 km^2 (continental scale) down to $\approx 0.01\,\text{km}^2$ (sub-block scale), where library and auto-bailout limits permitted. Because resolution indices are not comparable across grid architectures (e.g. ISEA4H resolution 9 (194.6 km^2) is geometrically distinct from H3 resolution 9 (0.1 km^2)) all cross-grid comparisons in this section use mean cell area (km²) as the common axis. The resolution-to-area mapping for each grid is provided in Appendix Table A2. Before any DGGS encoding, a DuckDB `ST_Intersects` join was executed to establish a deterministic vector baseline. Measured mean baselines were: Macro (1:50m) = 3.94 s, Macro (1:10m) = 14.77 s, Macro (Europe) = 5.77 s, and Micro (Urban) = 0.81 s. To keep the experiment tractable for computationally expensive implementations, an auto-bailout mechanism was applied after each resolution iteration completes. If the measured covering time for resolution level r exceeded the threshold of 1,800 s (30 minutes), the sweep was not extended to the next finer resolution level $r + 1$. This is conservative by design: because polygon covering complexity scales by the grid's aperture factor per resolution step (approximately ×4 for ISEA4H, ×7 for H3), a completed iteration that already exceeds the threshold guarantees that all subsequent finer resolutions would be strictly more expensive. Importantly, the iteration that triggered the bailout is retained in full in the results (i.e. it is not truncated), so reported covering times may exceed 1,800 s where a single iteration ran to completion. This threshold primarily affected ISEA4H at fine resolutions, whose custom Python rasterizer lacks a native C-accelerated polyfill (Section 3.4.3)

4.5.2 Spatial Capture Accuracy. Accuracy in this context is the fraction of cell-encoded points assigned to a polygon by the DGGS equi-join relative to the floating-point `ST_Intersects` ground truth, where 100% denotes perfect agreement. Figure 8 plots accuracy as a function of mean cell area (km^2) across the four evaluation scopes.

Tier 1 — Industry DGGS. Both H3 and S2 converge rapidly toward $\geq$ 99% accuracy at mid-range resolutions across all four scopes. H3 reaches this threshold at coarser cell sizes than S2 in all cases, consistent with its lower normalized area variance documented in Section 4.2. Neither grid exhibits overcounting at any evaluated resolution.

Tier 2 — Academic DGGS. rHEALPix converges more slowly than the $T1$ grids, particularly at the Macro (1:10m) and Europe scopes, where the equal-area boundary constraints generate more ambiguous cell assignments at coarser resolutions before converging above 99%. ISEA4H presents a distinct pattern: at coarse resolutions, accuracy ranges from 90% to 96% across scales, reflecting partial polygon coverage from its custom centroid-filter rasterizer. At fine resolutions, accuracy climbs to 99.2%–99.7% (Macro scopes) and 100.0% (Micro Urban). Critically, ISEA4H does not overcount: the centroid-inside-polygon post-filter ensures accuracy remains at or below the ground-truth ceiling at all resolutions. The lower accuracy at coarse scales reflects deliberate under-coverage rather than boundary bleed.

Tier 3 — Legacy Planar Grids. Both Geohash and XYZ Tiles persistently overcount at all tested resolutions. XYZ's inclusive `mercantile.tiles()` algorithm produces overcounting that ranges from 117% at coarse resolutions to 100.4% at the finest tested (resolution 17, 0.01 km^2), never converging to the ground-truth ceiling. Geohash shows the same structural behavior, with accuracy ranging from 106% to 100.2% across resolutions 4–7. At resolution 7 (0.6 km^2), Geohash reaches 100.23% (the closest approach to the ceiling of these grids), which we treat as a marginal operating point and include in the relational analysis (Table 4). XYZ is excluded from that analysis due to 1) its failure to converge within the tested resolution range and 2) since their spatial index is a three-component tuple `(z, x, y)` rather than a scalar cell identifier. Both grids are presented separately in Appendix Figure A5.

4.5.3 Polygon Covering Efficiency (The ETL Tax). Converting a floating-point vector polygon into a DGGS cell identifier set is the primary upfront latency barrier of any DGGS workflow. This has no vector equivalent as it is pure overhead (the "ETL Tax") that must be amortized across

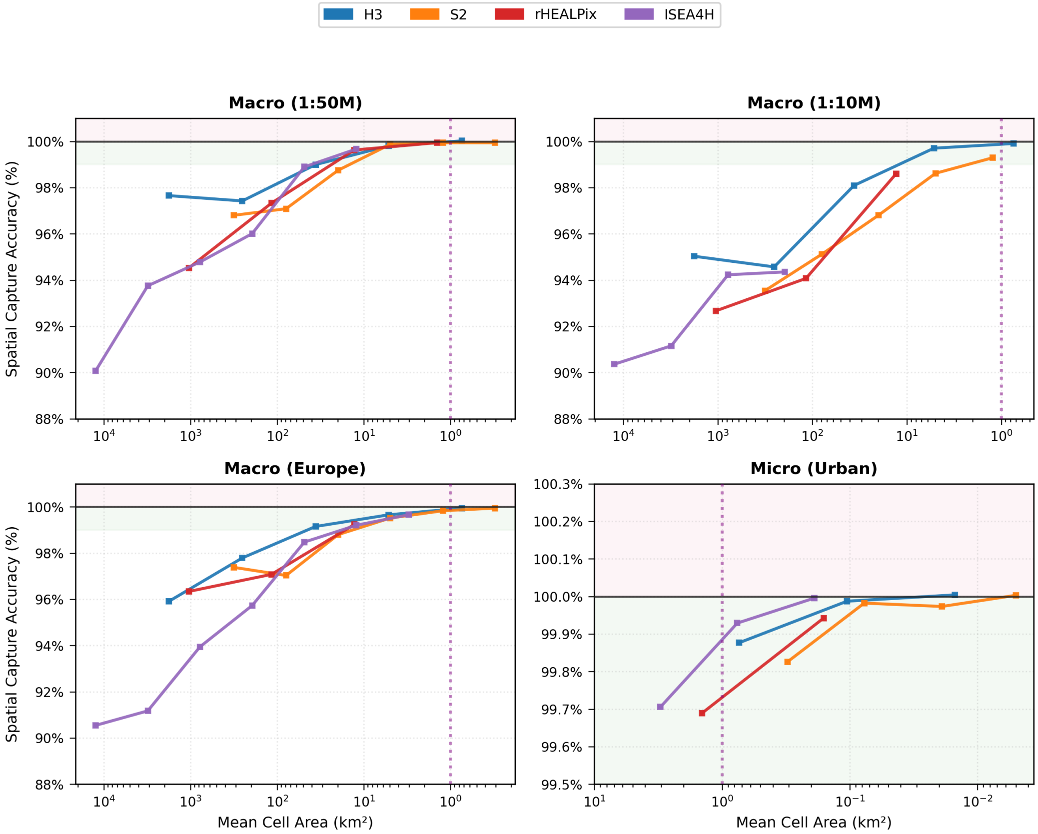

Fig. 8. Spatial capture accuracy of DGGS as a function of mean cell area. The vertical dashed line highlights 1km^2 cell area, while the green background highligts 99% capture accuracy. Note that both vertical and horizontal scales are diferent for the Urban scope.

subsequent queries. Figure 9 plots covering time against mean cell area on log–log axes across the four evaluation scopes. The log–log linearity confirms consistent power-law scaling across all grids. Covering time T scales with cell area A as $T = k \cdot A^{\beta}$ (for a grid- and polygon-specific constant k), where the fitted exponent $\beta < 0$ is annotated directly on each regression line in the figure. Because β is negative, finer resolutions always incur disproportionately higher covering costs. A halving of cell size increases covering time by approximately $2^{|\beta|}$, which corresponds to the observed 2.5×–4.0× range across grids. This linear scaling means that the ETL Tax cannot be avoided by modestly increasing resolution: each step finer compounds the covering cost by the grid's aperture factor.

Tier 1 — Industry DGGS. H3, with a native C-compiled polyfill, achieves the lowest covering times at any given cell size. At Macro (1:50m) resolution 8 (0.74 km^2), H3 covers five global countries in 98.9 s; at Macro (Europe), the 15-country footprint takes only 10.4 s at the same resolution — faster despite more polygons, because European country extents are smaller and less vertex-dense. S2's Python-layer `RegionCoverer` is substantially slower: 3,598 s at Macro (1:50m), requiring resolution 13 (0.31 km^2) to achieve comparable accuracy. The Coastline Paradox is quantitatively isolated by the Macro (1:50m) vs. Macro (1:10m) contrast. For H3, covering the same five countries at finer boundary resolution (0.74 km^2, fixed cell size) increases covering time from 98.9 s to 392.9 s — a 4.0× increase attributable entirely to boundary vertex density, independent of geographic area.

paragraphTier 2 — Academic DGGS Both rHEALPix and ISEA4H lack native polyfill implementations and rely on custom Python rasterizers that densify polygon boundaries, encode candidate points, and filter by centroid containment — all in interpreted code. rHEALPix covering at Macro (1:50m) resolution 8 takes 15,258 s, which is 154× slower than H3 at comparable cell size (1.44 vs. 0.74 km^2). ISEA4H covering ranges from 74.0 s (Micro Urban, resolution 14) to 4,807 s (Macro 1:50m, resolution 11). The Macro (1:10m) ISEA4H sweep reaches the 1,800 s auto-bailout threshold at resolution 9 (194.6 km^2), leaving finer resolutions unevaluated for that scope.

Tier 3 — Legacy Planar Grid. Geohash covering via `polygon_geohasher` produces moderate times: 612.6 s at Macro (1:50m) and 136.8 s at Macro (Europe) — slower than H3 at similar cell areas but faster than the Academic DGGS, reflecting the intermediate complexity of the recursive base-32 boundary traversal. XYZ covering is excluded from this analysis as the grid is not evaluated at operating points.

4.5.4 Relational Break-Even & Throughput Analysis. Table 4 presents, for each grid and evaluation scope, the peak-accuracy operating point, the polygon covering ETL cost, the pre-computed equi-join time, the resulting speedup over the `ST_Intersects` vector baseline, and the break-even query count N — the minimum number of repeated queries against the same pre-computed index at which the total pipeline cost (covering + N joins) falls below the cost of N direct vector joins. ISEA4H vector baselines are normalized to the canonical per-scale means from the H3/S2/rHEALPix batch runs (4.40 s, 13.70 s, 5.90 s, 0.81 s) so that speedup and break-even figures are directly comparable across all grids. Figure 10 visualizes the same operating points as stacked execution bars.

Three findings emerge from Table 4 and Figure 10. First, pre-computed DGGS joins universally outperform vector baselines. All five grids execute sub-second equi-joins across all scopes. Speedups range from 13× (H3, Micro Urban) to 457× (ISEA4H, Macro 1:10m), with the largest gains where the `ST_Intersects` baseline is most expensive relative to the equi-join latency. This confirms that DGGS relational indexing is viable as a replacement for vector join operations once the cell index is materialized.

Second, on-the-fly covering is not competitive with vector joins at macro scales. Even H3's fastest macro covering (10.4 s, Europe) exceeds its vector baseline (5.90 s) by 1.8×. The Academic DGGS covering times — measured in thousands of seconds — make cold-start queries operationally infeasible at macro scales. This establishes a mandatory architectural constraint: DGGS spatial indexes must be pre-computed and persisted, and the ETL Tax is recoverable only if the index is queried multiple times.

Third, break-even thresholds are sensitive to resolution choice. Break-even N values reported in Table 4 correspond to peak-accuracy operating points and therefore represent the most ETL-intensive scenario for each grid. Stepping back one or two resolution levels — accepting cell sizes that are 4×–10× coarser — reduces covering cost dramatically while keeping spatial accuracy above 98%–99% in all cases. For H3 Macro (1:50m), this reduces break-even from 23 to 3 queries at resolution 7 (99.8% accuracy). For ISEA4H Macro (1:50m), break-even falls from 1,105 to 275 at resolution 10 (98.9% accuracy). The full resolution step-back trade-off for all grids is reported in Appendix Table A3.

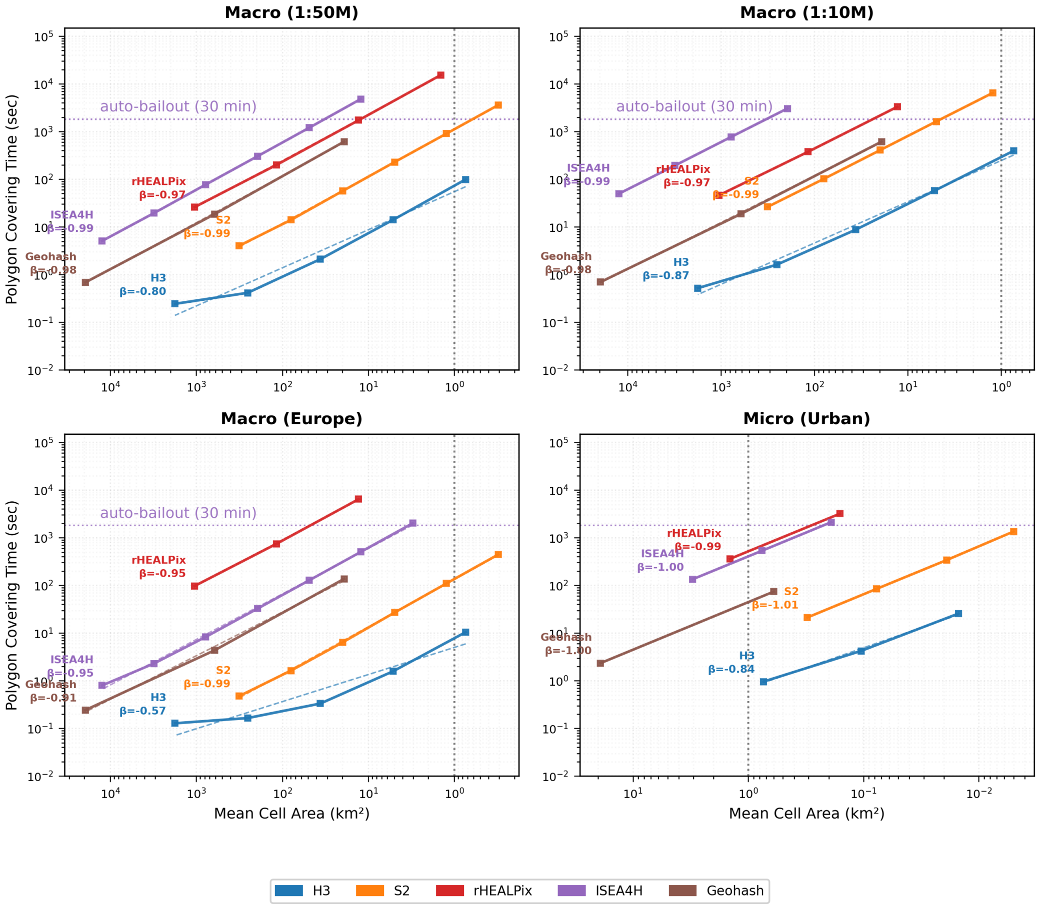

Fig. 9. Polygon covering latency (ETL Tax) on log–log axes across four evaluation scopes. The annotated β exponent quantifies the power-law scaling rate ($T \propto A^{\beta}$) for each grid. The vertical dotted line marks the 1 km^2 cell area reference threshold. The Macro (1:50m) vs. Macro (1:10m) panel pair shows that identical geographies at finer boundary resolution increase covering cost. ISEA4H's Macro (1:10m) sweep is truncated at resolution 9 (194.6 km^2) by the 1,800 s auto-bailout threshold.

5 Discussion of the Results

5.1 The Tier Taxonomy as a Proxy Framework

A central observation across all four experiments is that the three-tier classification introduced in Section 4.1 is not merely a descriptive label but a proxy framework. Tier membership, which reflects underlying design intent (production deployment vs. mathematical rigor vs. legacy convention), consistently anticipates the direction and approximate magnitude of performance differences across experiments that are otherwise methodologically independent. The taxonomy serves as a proxy to computational throughput results (Section 4.4): performance ordering strictly follows tier membership by backend binding depth. The same taxonomy also structures topological resilience ($T3$ fails at poles; $T1$ is globally uniform), geometric fidelity ($T2$ achieves zero area variance; $T3$ diverges at high latitudes), and relational accuracy ($T1$ converges earliest; $T2$ converges more

Table 4. Relational throughput at peak-accuracy operating points. Speedup is the ratio of the `ST_Intersects` vector baseline to the equi-join latency. Break-even N is the minimum number of repeated queries at which the total pipeline cost (covering + N joins) falls below N direct vector joins. ISEA4H baselines use canonical values normalized across grids (see Section 4.5).

Grid	Scale	Res.	Area (km^2)	Acc. (%)	Cover (s)	Join (s)	Speedup	B-E (N)
H3	Macro (1:50m)	8	0.74	100.0	98.9	0.153	29×	23
H3	Macro (1:10m)	8	0.74	99.9	392.9	0.144	95×	29
H3	Macro (Europe)	8	0.74	99.9	10.4	0.090	66×	2
H3	Micro (Urban)	10	0.02	100.0	25.6	0.069	13×	31
S2	Macro (1:50m)	13	0.31	99.9	3,598	0.154	29×	209
S2	Macro (1:10m)	12	1.23	99.3	6,460	0.072	190×	474
S2	Macro (Europe)	13	0.31	99.9	445.1	0.083	71×	76
S2	Micro (Urban)	16	<0.01	100.0	1,347	0.052	17×	1,596
rHEALPix	Macro (1:50m)	8	1.44	99.9	15,258	0.114	39×	3,561
rHEALPix	Macro (1:10m)	7	12.94	98.6	3,297	0.043	318×	241
rHEALPix	Macro (Europe)	7	12.94	99.2	6,424	0.043	137×	1,096
rHEALPix	Micro (Urban)	9	0.16	99.9	3,194	0.031	29×	3,692
ISEA4H	Macro (1:50m)	11	12.20	99.7	4,807	0.050	88×	1,105
ISEA4H	Macro (1:10m)†	9	194.60	94.4	3,037	0.030	457×†	222
ISEA4H	Macro (Europe)	12	3.04	99.7	2,012	0.055	107×	344
ISEA4H	Micro (Urban)	14	0.19	100.0	2,124	0.026	35×	2,430
Geohash	Macro (1:50m)	6	19.10	101.3	612.6	0.131	34×	143
Geohash	Macro (1:10m)	6	19.10	101.4	612.2	0.132	104×	45
Geohash	Macro (Europe)	6	19.10	100.9	136.8	0.099	60×	23
Geohash	Micro (Urban)	7	0.60	100.2	74.0	0.047	19×	87

†Auto-bailout triggered at resolution 9; resolutions 10–14 not evaluated. Speedup is a lower bound.

Geohash accuracy >100% reflects structural overcounting; included as a T3 reference operating point.

slowly; $T3$ overcounts structurally). Practitioners selecting a grid for a new analytical system can therefore use tier membership as a first-order filter before conducting grid-specific experiments with `dggs-bench`. It bears emphasising that the performance differences documented across tiers are not merely implementation artifacts. As stated in Section 4.1 and Section 3, each grid was evaluated using the best publicly available, actively maintained library at the time of writing — the tool a developer or researcher would realistically deploy today. Performance gaps therefore represent an accurate characterization of the real-world state of the DGGS ecosystem and available engineering resources, not a consequence of arbitrary library selection.

5.2 The Cost of Correctness: Area Fidelity vs. Operational Robustness

The four experiments together expose a consistent cost-quality trade-off that cuts across tiers. The $T2$ equal-area grids (rHEALPix, ISEA4H) achieve the highest geometric correctness — zero normalized area variance and strict cell congruence — at the cost of measurable operational penalties. rHEALPix exhibits the most extreme angular shear of any native DGGS ($\mu = 7.33^\circ$, max $= 59.91^\circ$, concentrated at the $\pm 41.81^\circ$ projection collar), a 9.2× latency swing between equatorial and polar zones ($d = 2.54$), and covering times up to 154× slower than H3 at comparable cell sizes.

The $T1$ grids (H3, S2) sacrifice area fidelity — cells range from 0.59× to 1.35× the mean cell area — but recover this cost through globally uniform computational behavior ($d = 0.01$ for H3 latency across zones), faster convergence to $\geq 99\%$ spatial accuracy, and access to compiled polyfills that

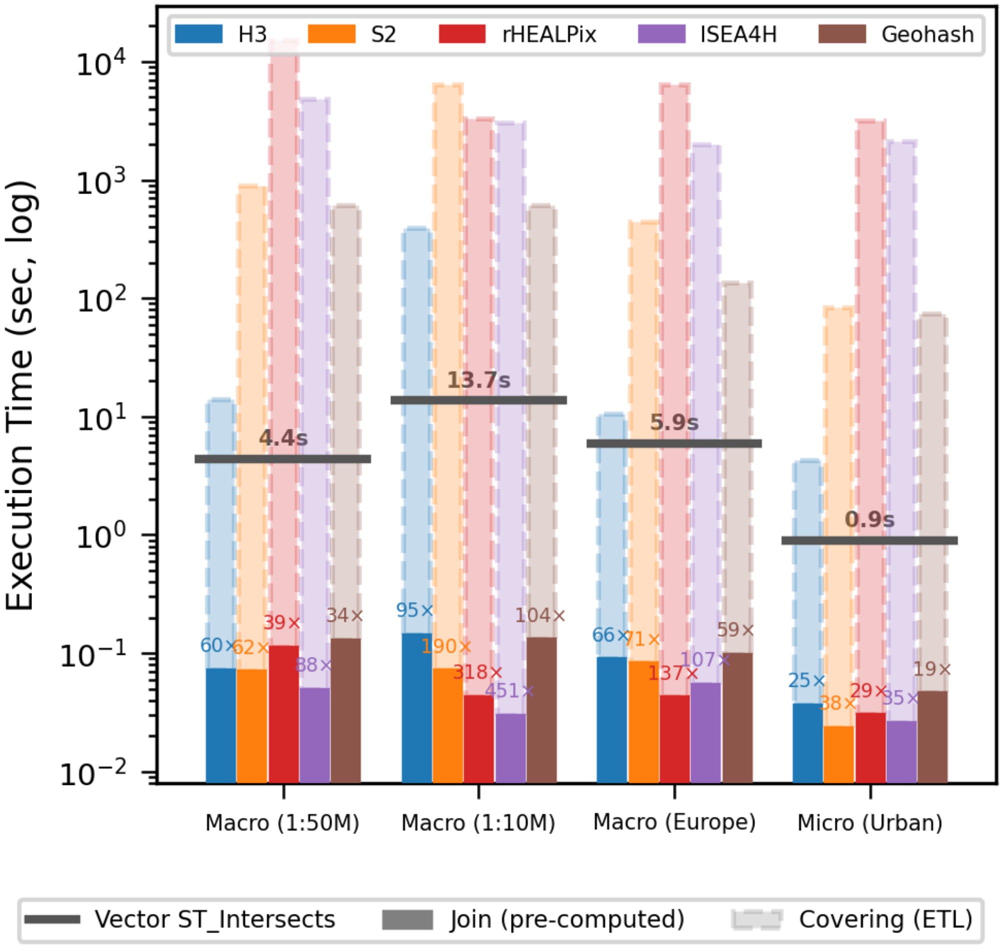

Fig. 10

reduce covering overhead by one to three orders of magnitude. The *T*3 planar grids represent the limit of this trade-off: arithmetic simplicity yields the highest raw throughput, but at the cost of structural overcounting, polar failure, and systematic area collapse. These are not implementation flaws — they are inevitable consequences of operating on a Euclidean plane. This trade-off has no universal resolution. Equal-area DGGS remain the correct choice where cell-level area equivalence is a scientific requirement (e.g., global biodiversity metrics, climate model grids). Industry DGGS are correct where operational uniformity and ecosystem maturity dominate the selection criteria. Legacy planar grids are defensible only where backward compatibility with existing tilemap or Geohash infrastructure is a hard constraint.

5.3 DGGS Ecosystem Gap

A broader finding of this study concerns the academic DGGS tier as a category. Both rHEALPix and ISEA4H demonstrate sound geometric properties by design (zero normalized area variance, strict equal-area enforcement, and full topological continuity across all singularity stress zones). Their equi-join latencies are also competitive: ISEA4H completes joins in 0.026–0.055 s and rHEALPix in 0.031–0.114 s, both well within the sub-second threshold across all four evaluation scopes. However, there is still a significant limitation in their ecosystem maturity. Neither academic grid has a native, compiled polygon polyfill. Both covering implementations are pure-Python rasterizers that densify polygon boundaries, invoke point encoding iteratively, and filter by containment. These operations are performed in compiled C via vectorized batch APIs by industry DGGS. The result is a covering overhead of 3,194–15,258 s for rHEALPix and 2,012–4,807 s for ISEA4H at macro scales. This makes cold-start indexing operationally infeasible for both. rHEALPix is additionally constrained by its pure-Python library architecture, which introduces a 9.2× encoding latency penalty at polar coordinates due to uncompiled projection-branch switching. For ISEA4H, the `pybind11` bridge to `dglib` developed as part of this work represents the highest-performance Python access currently available, and even so, the single missing component is a compiled covering algorithm.

This gap is not intrinsic to these grid architectures. As noted in [21], increasing structural fidelity inevitably raises computational and memory demands. Our benchmarks quantify this overhead as one to three orders of magnitude above industrial standards. But the overhead is attributable entirely to the absence of compiled tooling, not to the grids' mathematical properties. A production-grade polyfill for either grid would likely bring covering performance to within one order of magnitude of H3. This is the same gap that separates `s2sphere` (pure Python) from a native S2 binding in our computational latency results. The academic DGGS community has produced geometrically rigorous systems; the open engineering gap is in the deployment infrastructure.

5.4 ETL Tax, Break-Even, and the Path to Pre-Indexed Data

The break-even analysis (Table 4, Appendix Table A3) clarifies a constraint often stated qualitatively but not previously measured at scale: DGGS relational indexing is exclusively an *OLAP* (batch pre-computed) pattern, not an *OLTP* (on-the-fly transactional) one. Even for H3, on-the-fly macro-scale covering (98.9 s) exceeds the direct vector baseline (4.40 s) by 22×; the ETL Tax is recoverable only through repeated queries against the same pre-computed index. However, break-even thresholds are highly sensitive to resolution choice and should not be treated as fixed constraints. As illustrated in Table 5 for H3 and ISEA4H, stepping back one resolution level — accepting cell sizes 4×–10× coarser while keeping accuracy above 98%–99% — reduces break-even dramatically. For H3, the threshold falls from 23 to 3 queries; for ISEA4H, from 1,105 to 275. Practitioners can therefore treat N as a tunable deployment parameter, selecting the coarsest resolution that meets their application's accuracy floor.

The universal performance gains observed in our pre-computed equi-joins—achieving sub-second latencies across all scopes—confirm that DGGS relational indexing is a viable alternative to complex vector join operations in modern analytical engines. This finding aligns with earlier results from the IDEAS platform [42], which reported superior performance for discrete space representations across varying data volumes within a relational environment . While IDEAS established this feasibility on specialized hardware like Netezza, our results demonstrate that these speedups are equally reproducible in lightweight, vectorized engines like DuckDB, even when scaling to 10-million-point joins.

A secondary deployment implication emerges from the parent-cell inversion finding (Section 4.4): vertical hierarchical traversal and horizontal spatial query are governed by entirely different implementation constraints. Grids with integer-arithmetic hierarchies (Geohash, ISEA4H, rHEALPix) outperform compiled DGGS (H3, S2) on parent-cell operations by 1.6×–5.0×, despite being substantially slower on encoding and k-ring queries. Analytical systems that rely on multi-resolution drill-down should weight this inversion in their grid selection criteria.

Table 5. Resolution step-back: break-even N for H3 and ISEA4H (Macro 1:50m). Full resolution sweep for all grids in Appendix Table A3.

Grid	**Step**	**Res.**	**Area (km^2)**	**Acc. (%)**	**B-E (N)**
H3	Peak	8	0.74	100.0	23
	−1	7	5.16	99.8	**3**
	−2	6	36.10	99.0	**1**
ISEA4H	Peak	11	12.20	99.7	1,105
	−1	10	48.60	98.9	**275**

Finally, it is worth noting that the ETL Tax documented here is a transition cost, not a permanent one. As geospatial datasets increasingly ship with pre-computed DGGS cell identifiers, the covering step moves from a per-deployment burden to a one-time upstream infrastructure investment. FourSquare operates the H3 Hub [1] that provides free access to over 70 geospatial datasets pre-indexed with H3 cells, and platforms such as Google BigQuery, Snowflake, Carto also now expose native H3 indexes. For datasets that arrive pre-indexed, the relational reward (13×–457× speedup) is immediately accessible with no ETL cost whatsoever, rendering the break-even analysis moot.

Beyond throughput, DGGS cell identifiers carry structural properties that vector geometries cannot provide. Because each identifier is permanently and globally assigned to a fixed area of the Earth's surface, DGGS indices act as persistent spatio-temporal keys. Two observations from different epochs, sensors, or datasets assigned to the same cell ID are unambiguously co-located without any spatial join or coordinate reconciliation. This makes DGGS a natural fit for longitudinal change analysis and data fusion workflows, where the traditional approach requires repeated re-alignment of incompatible grids, coordinate systems, or raster extents. The hierarchical parent–child relationships further enable native multi-resolution aggregation,

5.5 Limitations

Several limitations bound the generalizability of these results. First, all experiments were executed on a single consumer workstation (64 GB RAM, 24-core AMD Ryzen CPU). Distributed and cloud-native execution environments — where memory bandwidth, network I/O, and node coordination introduce additional overhead — may alter the relative performance ordering, particularly for covering-heavy Academic DGGS workloads.

Second, S2 was evaluated via `s2sphere`, the most widely adopted and stable Python interface for S2 at the time of writing. Google's SWIG-bound native binding (`s2geometry`) would likely achieve encoding throughput closer to H3, but is explicitly flagged as unstable in the official repository documentation and is not widely deployed in production systems. `s2sphere` therefore represents the most realistic S2 deployment scenario available, and its results should be interpreted accordingly.

Third, the relational throughput experiment used Foursquare Open Source Places as the point dataset, which reflects a real-world but non-uniform POI spatial distribution concentrated in urban areas. Workloads with uniform or raster-origin point distributions may exhibit different capture accuracy trajectories, particularly at coarse resolutions where urban clustering can bias containment counts.

Fourth, break-even thresholds are computed at peak-accuracy operating points and therefore represent the most ETL-intensive scenario for each grid. As demonstrated in Appendix Table A3, accepting marginally coarser resolution reduces these thresholds substantially — a dimension of the deployment trade-off space that practitioners should explore with `dggs-bench` for their specific accuracy requirements.

Finally, the ISEA4H Macro (1:10m) resolution sweep was terminated by the 1,800 s auto-bailout at resolution 9 (194.6 km^2), leaving resolutions 10–14 unmeasured for that scope. The reported ISEA4H speedup for Macro (1:10m) (487×) should therefore be interpreted as a lower bound on the achievable speedup at finer resolutions, where join times remain sub-second while the vector baseline (14.77 s) remains constant.

6 Summary and Future Work

This paper presented a systematic, reproducible, multi-experiment evaluation of six geospatial indexing implementations spanning the full architectural spectrum of modern spatial indexing. Four Discrete Global Grid Systems (H3, S2, rHEALPix, and ISEA4H) and two legacy planar grids (XYZ Tiles and Geohash) were evaluated across geometric fidelity, topological resilience, computational throughput, and relational database performance. Each grid was assessed using the best publicly available and actively maintained library at the time of writing, ensuring that results reflect the real-world state of the ecosystem rather than a laboratory idealization. The principal contributions are:

- `dggs-bench` [23] Framework: An open-source, portable benchmarking utility featuring a universal abstraction layer (`BaseGrid`) that standardizes spatial operations across disparate grid libraries — from Cython-compiled C-cores to pure-Python implementations and custom C++ bridges. The unified API contract allows researchers to evaluate emerging grid implementations against established baselines without modifying the core framework, while a decoupled execution pipeline ensures reproducibility across computing environments.
- First Systematic ISEA4H Benchmark: The first end-to-end evaluation of ISEA4H, enabled by a custom `pybind11` bridge to the `dglib` C++ library developed as part of this work, filling a significant gap in the academic DGGS benchmarking literature.
- Four-Experiment Evaluation Protocol: A comprehensive protocol quantifying geometric fidelity, topological resilience at geographic singularities, computational throughput, and relational database performance — the first benchmark to cover all four dimensions simultaneously across six representative implementations.
- Empirical ETL Cost and Break-Even Quantification: The first systematic measurement of the upfront polygon covering cost, its power-law scaling with resolution, and the minimum query count required to recover the ETL investment for each grid and evaluation scope.

The following key findings connect theoretical grid properties with real-world system performance, providing decision-support for software architects, geospatial scientists, and Digital Earth practitioners:

- Pre-computed DGGS joins universally outperform vector baselines: All evaluated grids complete 10,000,000-point equi-joins in under 200 ms, with speedups ranging from 13× (H3, Micro Urban) to 457× (ISEA4H, Macro 1:10m) over DuckDB `ST_Intersects` baselines. Relational hash-joins effectively decouple spatial query performance from polygon boundary complexity.
- The ETL Tax mandates pre-computation, but is resolution-tunable: On-the-fly polygon covering is not competitive with direct vector joins at macro scales for any grid. However, break-even query thresholds are sensitive to resolution choice: for H3 Macro (1:50m), accepting one coarser resolution level (99.8% accuracy) reduces break-even from 23 to 3 queries; for ISEA4H, from 1,105 to 275 at 98.9% accuracy.
- Performance rank is the inverse of geometric correctness: Throughput is governed by backend binding depth rather than grid quality. Legacy Planar grids achieve the highest raw encoding throughput precisely by forgoing spherical accuracy. A performance inversion

exists in vertical hierarchical traversal, where integer-arithmetic grids (ISEA4H, rHEALPix) reach 6.9–8.6 million parent operations/s, exceeding H3 and S2 despite lower encoding throughput.

- Geometric correctness comes at an operational cost: $T2$ equal-area grids achieve zero area distortion by construction, but at the cost of angular shear peaking at 59.91° (rHEALPix), latency instability of 9.2× across geographic zones ($d = 2.54$), and covering overhead up to 154× higher than H3 at comparable cell sizes. $T3$ planar grids fail entirely at polar zones ($> 85.05°$), confirming the structural limitations of operating on a Euclidean plane.
- The ecosystem gap is an engineering problem, not a geometric one: ISEA4H equi-join latency is competitive with H3 and S2 across all scopes, confirming that its spatial indexing is geometrically sound. The covering bottleneck is attributable entirely to the absence of a native compiled polyfill — a tooling investment gap that, if resolved, would bring ISEA4H within operational range for production deployments.

6.1 Future Work

Future research should prioritize determining if DGGS can definitively resolve the "planar fallacy" in global GeoAI foundations [24]. While evaluating DGGS as a native substrate for GeoAI workflows was beyond the scope of this benchmark study, the throughput and geometric fidelity results reported here provide the empirical foundation for such an investigation. Additionally, this study issues a call to action to address the maturity gap between mathematically sound academic grids and industrial implementations. Developing C-accelerated polyfills and high-performance bindings for ISEA4H, rHEALPix and other grids is a prerequisite for their adoption in production-scale pipelines. Finally, extending `dggs-bench` to cloud-native distributed environments and exploring dynamic multi-resolution query planning based on boundary complexity remain systems design challenges.

Data Availability

The experimental datasets supporting the findings of this study are openly available on OSF at https://doi.org/10.17605/OSF.IO/BZKX6, including all four benchmark result files in Parquet format, the master analysis notebook (`TSAS_2026_Master.ipynb`), and a pre-rendered HTML version of all figures. The `dggs-bench` benchmarking framework is released as open-source software under the MIT License at https://github.com/gatorlab-geo/dggs-bench.

References

[1] [n. d.]. Spatial H3 Hub. https://docs.foursquare.com/analytics-products/docs/fsq-spatial-h3-hub-getting-started

[2] 2021. Geographic information — Discrete Global Grid Systems Specifications Part 1: Core Reference System and Operations, and Equal Area Earth Reference Syste.

[3] 2026. GBIF.org. https://www.gbif.org/

[4] Troy Alderson, Matthew Purss, Xiaoping Du, Ali Mahdavi-Amiri, and Faramarz Samavati. 2020. Digital Earth Platforms. In *Manual of Digital Earth*, Huadong Guo, Michael F. Goodchild, and Alessandro Annoni (Eds.). Springer, Singapore, 25–54. doi:10.1007/978-981-32-9915-3_2

[5] Ben Bondaruk, Steven A. Roberts, and Colin Robertson. 2020. Assessing the state of the art in Discrete Global Grid Systems: OGC criteria and present functionality1. *Geomatica* 74, 1 (March 2020), 9–30. doi:10.1139/geomat-2019-0015

[6] Boyuan, Guan, Wencong Cui, and Levente Juhasz. 2026. A Dual-Helix Governance Approach Towards Reliable Agentic AI for WebGIS Development. doi:10.48550/arXiv.2603.04390 arXiv:2603.04390 [cs].

[7] Isaac Brodsky. 2018. H3: Uber's Hexagonal Hierarchical Spatial Index. https://www.uber.com/us/en/blog/h3/

[8] Christopher F. Brown, Michal R. Kazmierski, Valerie J. Pasquarella, William J. Rucklidge, Masha Samsikova, Chenhui Zhang, Evan Shelhamer, Estefania Lahera, Olivia Wiles, Simon Ilyushchenko, Noel Gorelick, Lihui Lydia Zhang, Sophia Alj, Emily Schechter, Sean Askay, Oliver Guinan, Rebecca Moore, Alexis Boukouvalas, and Pushmeet Kohli. 2025.

AlphaEarth Foundations: An embedding field model for accurate and efficient global mapping from sparse label data. doi:10.48550/arXiv.2507.22291 https://doi.org/10.48550/arXiv.2507.22291.

[9] Dan Carr, Ralph Kahn, Kevin Sahr, and Tony Olsen. 1997. ISEA Discrete Global Grids. *Statistical Computing & Statistical Graphics Newsletter* 8, 2/3 (1997), 31–39. https://mason.gmu.edu/~dcarr/lib/v8n2.pdf

[10] Jacob Cohen. 2013. *Statistical Power Analysis for the Behavioral Sciences* (2 ed.). Routledge, New York. doi:10.4324/9780203771587

[11] Martin Davis. [n. d.]. GEOS: geos::algorithm::RayCrossingCounter Class Reference. https://libgeos.org/doxygen/classgeos_1_1algorithm_1_1RayCrossingCounter.html

[12] Yuanzheng Duan, Xuesheng Zhao, Wenbin Sun, Qingping Liu, and Mengmeng Qin. 2024. A multimetric evaluation method for comprehensively assessing the influence of the icosahedral diamond grid quality on SCNN performance. *International Journal of Digital Earth* 17, 1 (Dec. 2024), 2313313. doi:10.1080/17538947.2024.2313313 _eprint: https://doi.org/10.1080/17538947.2024.2313313.

[13] R G Gibb. 2016. The rHEALPix Discrete Global Grid System. *IOP Conference Series: Earth and Environmental Science* 34, 1 (April 2016), 012012. doi:10.1088/1755-1315/34/1/012012

[14] Robert G. Gibb, Matthew B.J. Purss, Zoheir Sabeur, Peter Strobl, and Tengteng Qu. 2022. Global Reference Grids for Big Earth Data. *Big Earth Data* 6, 3 (July 2022), 251–255. doi:10.1080/20964471.2022.2113037 _eprint: https://doi.org/10.1080/20964471.2022.2113037.

[15] Álvaro González. 2010. Measurement of Areas on a Sphere Using Fibonacci and Latitude–Longitude Lattices. *Mathematical Geosciences* 42, 1 (Jan. 2010), 49–64. doi:10.1007/s11004-009-9257-x

[16] Michael F. Goodchild. 1994. Criteria for evaluation of global grid models for environmental monitoring and analysis.

[17] Michael F. Goodchild. 2018. Reimagining the history of GIS. *Annals of GIS* 24, 1 (Jan. 2018), 1–8. doi:10.1080/19475683.2018.1424737 _eprint: https://doi.org/10.1080/19475683.2018.1424737.

[18] Boyuan (Keven) Guan. 2025. Agentic-AI Lab: Engineering the Next Generation of Intelligent Systems. doi:10.5281/zenodo.17561541

[19] Antonin Guttman. 1984. R-trees: a dynamic index structure for spatial searching. In *Proceedings of the 1984 ACM SIGMOD international conference on Management of data (SIGMOD '84)*. Association for Computing Machinery, New York, NY, USA, 47–57. doi:10.1145/602259.602266

[20] Stefan Hahmann and Dirk Burghardt. 2013. How much information is geospatially referenced? Networks and cognition. *International Journal of Geographical Information Science* 27, 6 (June 2013), 1171–1189. doi:10.1080/13658816.2012.743664 _eprint: https://doi.org/10.1080/13658816.2012.743664.

[21] Xinhai Huang, Junjie Ding, Jin Ben, Jianbin Zhou, Qishuang Liang, and Jinchi Dai. 2024. Advancing digital earth modeling: Hexagonal multi-structural elements in icosahedral DGGS for enhanced geospatial data processing. *Environmental Modelling & Software* 172 (Jan. 2024), 105922. doi:10.1016/j.envsoft.2023.105922

[22] International Organization for Standardization. 2021. ISO 19170-1:2021 Geographic information - Discrete Global Grid Systems Specifications. https://www.iso.org/standard/32588.html https://www.iso.org/standard/32588.html.

[23] Levente Juhász. 2026. `dggs-bench`*: A Reproducible Benchmarking Framework for Discrete Global Grid Systems*. https://github.com/gatorlab-geo/dggs-bench

[24] Levente Juhász. 2026. Discrete Global Grid Systems as a Framework for Geometrically Rigorous and Spatially Explicit GeoAI: A Research Agenda. doi:10.5281/zenodo.18471033

[25] Levente Juhász. 2026. Replication Data: A Systematic Benchmark Across Geometry, Computation and Relational Joins. doi:10.17605/OSF.IO/BZKX6 Accessed: 2026.

[26] Gregory M. Kapfhammer. 2025. SE Radio 694: Jennings Anderson and Amy Rose on Overture Maps. https://se-radio.net/2025/11/se-radio-694-jennings-anderson-and-amy-rose-on-overture-maps/

[27] Jon A. Kimerling, Kevin Sahr, Denis White, and Lian Song. 1999. Comparing Geometrical Properties of Global Grids. *Cartography and Geographic Information Science* 26, 4 (Jan. 1999), 271–288. doi:10.1559/152304099782294186 _eprint: https://doi.org/10.1559/152304099782294186.

[28] Alexander Kmoch, Ivan Vasilyev, Holger Virro, and Evelyn Uuemaa. 2022. Area and shape distortions in open-source discrete global grid systems. *Big Earth Data* 6, 3 (July 2022), 256–275. doi:10.1080/20964471.2022.2094926 https://doi.org/10.1080/20964471.2022.2094926.

[29] Mingke Li, Heather McGrath, and Emmanuel Stefanakis. 2022. Multi-resolution topographic analysis in hexagonal Discrete Global Grid Systems. *International Journal of Applied Earth Observation and Geoinformation* 113 (Sept. 2022), 102985. doi:10.1016/j.jag.2022.102985

[30] Wenwen Li. 2025. Artificial Intelligence in Earth Science: A GeoAI Perspective. *Journal of Geophysical Research: Machine Learning and Computation* 2, 3 (2025), e2025JH000691. doi:10.1029/2025JH000691 _eprint: https://agupubs.onlinelibrary.wiley.com/doi/pdf/10.1029/2025JH000691.

[31] Yuqin Li, Jining Yan, Xiaohui Huang, Xiangyou He, Ze Deng, and Yunliang Chen. 2025. R-MLGTI: A Grid- and R-Tree-Based Hybrid Index for Unevenly Distributed Spatial Data. *ISPRS International Journal of Geo-Information* 14, 6

(June 2025), 231. doi:10.3390/ijgi14060231

[32] Yue Ma, Guoqing Li, Long Zhao, and Xiaochuang Yao. 2025. A Novel Earth-System Spatial Grid Model: ISEA4H-ESSG for Multi-Layer Geoscience Data Integration and Analysis. *Applied Sciences* 15, 7 (Jan. 2025), 3703. doi:10.3390/app15073703

[33] Benoit Mandelbrot. 1967. How Long Is the Coast of Britain? Statistical Self-Similarity and Fractional Dimension. *Science* 156, 3775 (May 1967), 636–638. doi:10.1126/science.156.3775.636

[34] Joan Masó, Keith Pomakis, and Núria Julià. 2010. OpenGIS Web Map Tile Service Implementation Standard v1.0.0.

[35] Gustavo Niemayer. 2008. geohash.org is public! https://web.archive.org/web/20080305223755/http://blog.labix.org/#post-85

[36] Laurens J. N. Oostwegel, Danijel Schorlemmer, and Philippe Guéguen. 2025. From Footprints to Functions: A Comprehensive Global and Semantic Building Footprint Dataset. *Scientific Data* 12, 1 (Oct. 2025), 1699. doi:10.1038/s41597-025-06132-z

[37] Shreyas Pangavhane, Gokul Raktate, Prasad Pariane, Krishna Shelar, Rohit Wakchaure, and J.N. Kale. 2024. AI-Augmented Software Development: Boosting Efficiency and Quality. In *2024 International Conference on Decision Aid Sciences and Applications (DASA)*. 1–5. doi:10.1109/DASA63652.2024.10836523

[38] Yongxin Peng. 2025. RL-RTree: A Reinforcement Learning-Optimized Dynamic R-Tree for High-Dimensional Spatial Indexing. *IEEE Access* 13 (2025), 114346–114355. doi:10.1109/ACCESS.2025.3583701

[39] Matthew B.J. Purss, Perry R. Peterson, Peter Strobl, Clinton Dow, Zoheir A. Sabeur, Robert G. Gibb, and Jin Ben. 2019. Datacubes: A Discrete Global Grid Systems Perspective. *Cartographica* 54, 1 (March 2019), 63–71. doi:10.3138/cart.54.1.2018-0017

[40] Mark Raasveldt and Hannes Mühleisen. 2019. DuckDB: an Embeddable Analytical Database. In *Proceedings of the 2019 International Conference on Management of Data (SIGMOD '19)*. Association for Computing Machinery, New York, NY, USA, 1981–1984. doi:10.1145/3299869.3320212

[41] Robert G. Raskin. 1994. Spatial Analysis on the Sphere: A Review (94-7). (Oct. 1994). https://escholarship.org/uc/item/5748n2xz

[42] Colin Robertson, Chiranjib Chaudhuri, Majid Hojati, and Steven A. Roberts. 2020. An integrated environmental analytics system (IDEAS) based on a DGGS. *ISPRS Journal of Photogrammetry and Remote Sensing* 162 (April 2020), 214–228. doi:10.1016/j.isprsjprs.2020.02.009

[43] Kevin Sahr. 2026. sahrk/DGGRID. https://github.com/sahrk/DGGRID original-date: 2019-09-03T21:15:20Z.

[44] Kevin Sahr, Denis White, and A. Jon Kimerling. 2003. Geodesic Discrete Global Grid Systems. *Cartography and Geographic Information Science* 30, 2 (Jan. 2003), 121–134. doi:10.1559/152304003100011090 _eprint: https://doi.org/10.1559/152304003100011090.

[45] Johannes Schmude, Sujit Roy, Will Trojak, Johannes Jakubik, Daniel Salles Civitarese, Shraddha Singh, Julian Kuehnert, Kumar Ankur, Aman Gupta, Christopher E. Phillips, Romeo Kienzler, Daniela Szwarcman, Vishal Gaur, Rajat Shinde, Rohit Lal, Arlindo Da Silva, Jorge Luis Guevara Diaz, Anne Jones, Simon Pfreundschuh, Amy Lin, Aditi Sheshadri, Udaysankar Nair, Valentine Anantharaj, Hendrik Hamann, Campbell Watson, Manil Maskey, Tsengdar J. Lee, Juan Bernabe Moreno, and Rahul Ramachandran. 2024. Prithvi WxC: Foundation Model for Weather and Climate. doi:10.48550/arXiv.2409.13598 https://doi.org/10.48550/arXiv.2409.13598.

[46] M. Shimrat. 1962. Algorithm 112: Position of point relative to polygon. *Commun. ACM* 5, 8 (Aug. 1962), 434. doi:10.1145/368637.368653

[47] Richard Swinbank and R. James Purser. 2006. Fibonacci grids: A novel approach to global modelling. *Quarterly Journal of the Royal Meteorological Society* 132, 619 (2006), 1769–1793. doi:10.1256/qj.05.227 _eprint: https://rmets.onlinelibrary.wiley.com/doi/pdf/10.1256/qj.05.227.

[48] Eric Veach. 2017. Announcing the S2 Library: Geometry on the Sphere S2 Geometry. https://opensource.googleblog.com/2017/12/announcing-s2-library-geometry-on-sphere.html

[49] Sophie Wagner, Fabian Stenzel, Tobias Krueger, and Jana de Wiljes. 2024. Drivers of global irrigation expansion: the role of discrete global grid choice. *Hydrology and Earth System Sciences* 28, 22 (Nov. 2024), 5049–5068. doi:10.5194/hess-28-5049-2024

[50] Xiaochuang Yao, Guoqing Li, Junshi Xia, Jin Ben, Qianqian Cao, Long Zhao, Yue Ma, Lianchong Zhang, and Dehai Zhu. 2020. Enabling the Big Earth Observation Data via Cloud Computing and DGGS: Opportunities and Challenges. *Remote Sensing* 12, 1 (Jan. 2020), 62. doi:10.3390/rs12010062

[51] Darius Šidlauskas, Simonas Šaltenis, and Christian S. Jensen. 2012. Parallel main-memory indexing for moving-object query and update workloads. In *Proceedings of the 2012 ACM SIGMOD International Conference on Management of Data (SIGMOD '12)*. Association for Computing Machinery, New York, NY, USA, 37–48. doi:10.1145/2213836.2213842

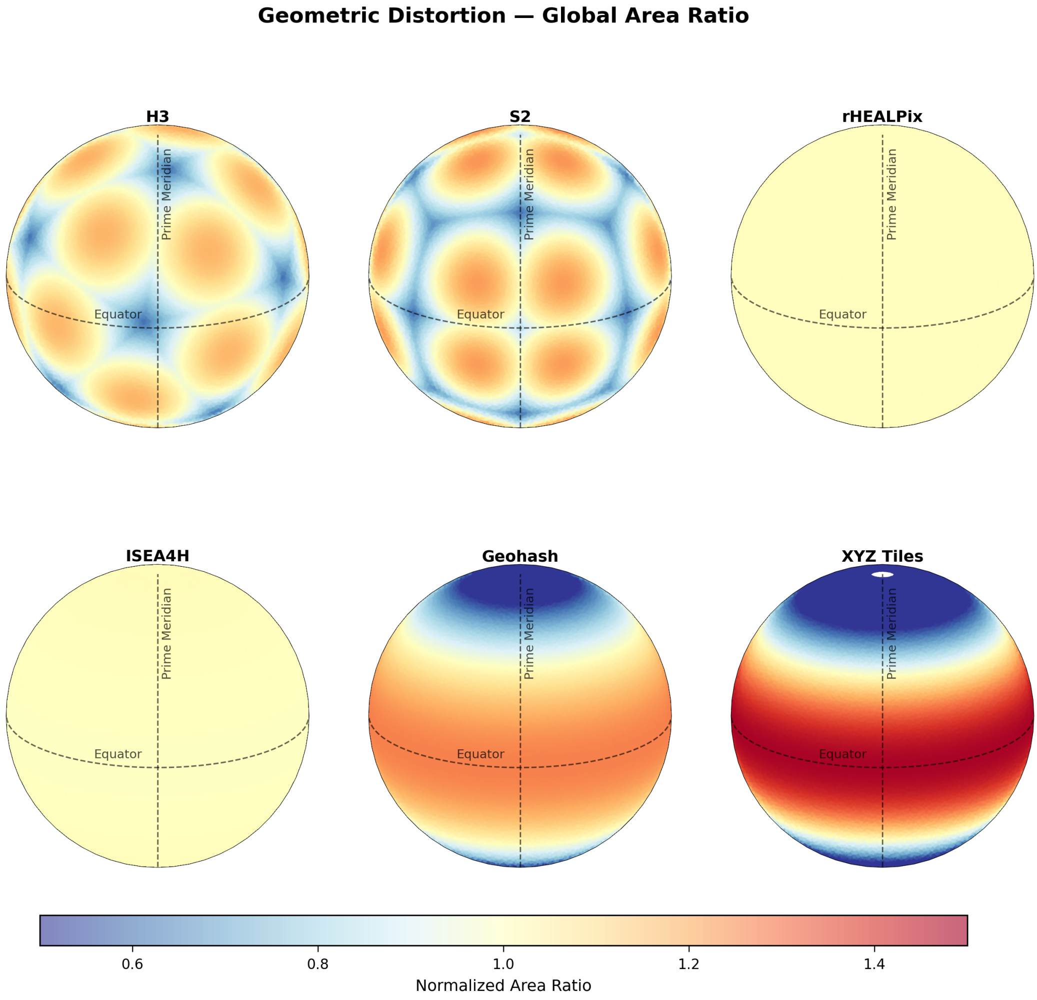

Fig. A1. Global Heatmaps mapping standardized area across grids.

7 Appendix

Received 30 April 2026; revised XX XX 2026; accepted YY YY 2026

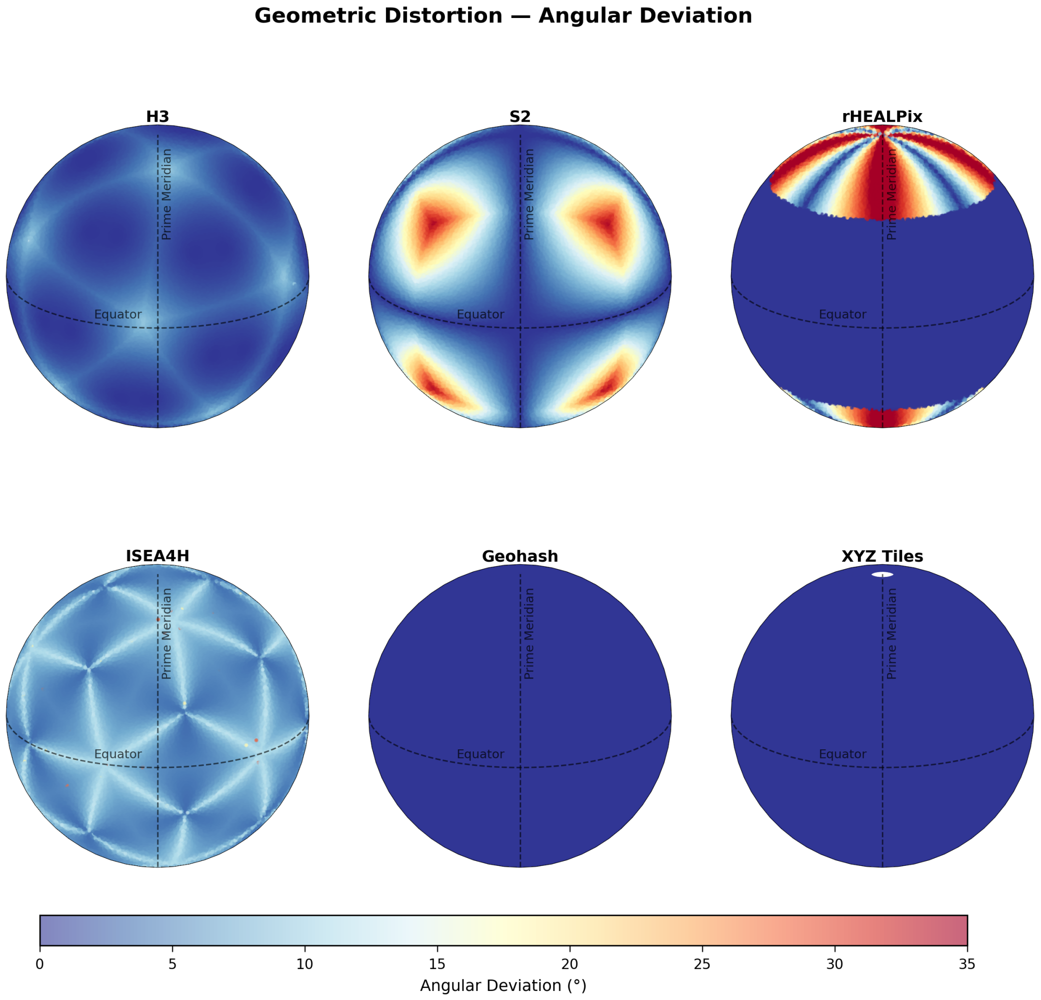

Fig. A2. Global Heatmaps mapping angular distortion

Table A1. Topological Resilience per zone (mean over 100,000 points). Spacing σ = std. dev. of neighbor centroid distances.

Grid	Zone	Survival	Latency (μs)	Spacing σ (m)	Neighbors[†]
H3	Control	100%	3.55	20.3	7
	Equator	100%	3.47	22.1	7
	Date Line	100%	3.55	27.4	7
	North Pole	100%	3.64	13.1	7
	South Pole	100%	3.40	13.1	7
S2	Control	100%	15.39	69.5	4
	Equator	100%	15.52	173.0	4
	Date Line	100%	15.70	178.5	4
	North Pole	100%	16.29	5.4	4
	South Pole	100%	15.25	5.4	4
rHEALPix	Control	100%	116.35	154.6	4
	Equator	100%	22.04	45.0	4
	Date Line	100%	106.66	92.7	4
	North Pole	100%	203.39	285.9	4
	South Pole	100%	209.16	274.0	4
ISEA4H	Control	100%	26.21	1011.7	6
	Equator	100%	25.93	767.0	6
	Date Line	100%	26.04	126.2	6
	North Pole	100%	24.36	746.5	6
	South Pole	100%	24.90	746.5	6
Geohash	Control	100%	2.05	228.7	9
	Equator	100%	2.05	334.8	9
	Date Line	100%	2.06	229.1	9
	North Pole	100%	2.02	279.3	9
	South Pole	100%	2.02	279.3	9
XYZ	Control	100%	2.75	761.4	8
	Equator	100%	2.76	1079.6	8
	Date Line	100%	2.82	642.2	8
	North Pole	**FAIL**	—	—	—
	South Pole	**FAIL**	—	—	—

[†] Neighbor count is the raw k-ring list length as returned by each library. H3 and Geohash include the origin cell in this list, inflating the count by 1.

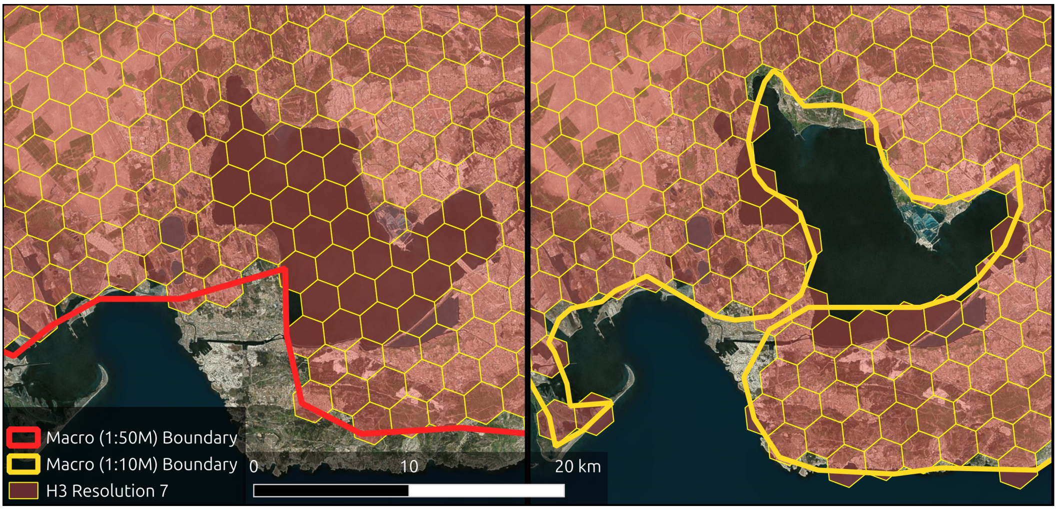

Fig. A3. Difference between Macro (1:50M) and Macro (1:10M) scales for the computational benchmark experiment.

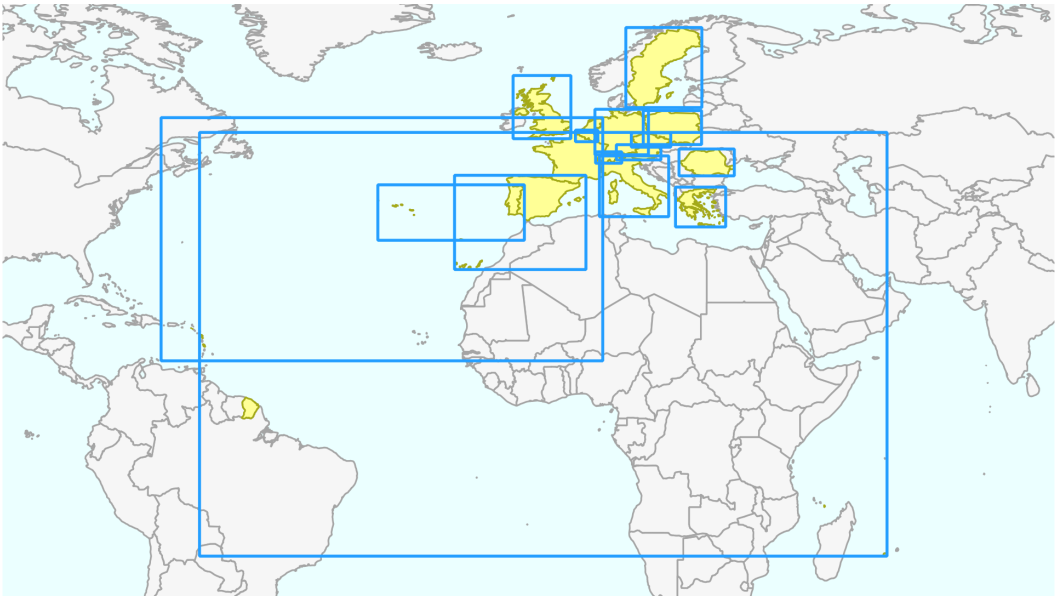

Fig. A4. Selected European countries for the computational throughout experiment (Macro (Europe) Scale) and their bounding boxes stress-testing R-Tree indexes.

Table A2. Resolution-to-cell-area mapping for all grids in the Relational Throughput experiment. Cell areas are global means. Geohash and XYZ Tiles are included for completeness; both exhibit persistent overcounting at all resolutions and are excluded from the operating point analysis.

H3		**S2**		**rHEALPix**		**ISEA4H**		**Geohash**		**XYZ**	
Res	km²	Res	km²	Res	km²	Res	km²	Res	km²	Res	km²
4	1,770	8	317.0	5	1,049	6	12,452	4	19,531	8	3,080
5	253	9	79.0	6	117	7	3,113	5	611	9	770
6	36	10	19.8	7	13	8	778	6	19	10	193
7	5.2	11	4.9	8	1.4	9	195	7	0.6	11	48
8	0.7	12	1.2	9	0.2	10	49			12	12
9	0.1	13	0.3			11	12			13	3.0
10	0.02	14	0.08			12	3.0			14	0.75
		15	0.02			13	0.8			15	0.19
		16	<0.01			14	0.2			16	0.05
										17	0.01

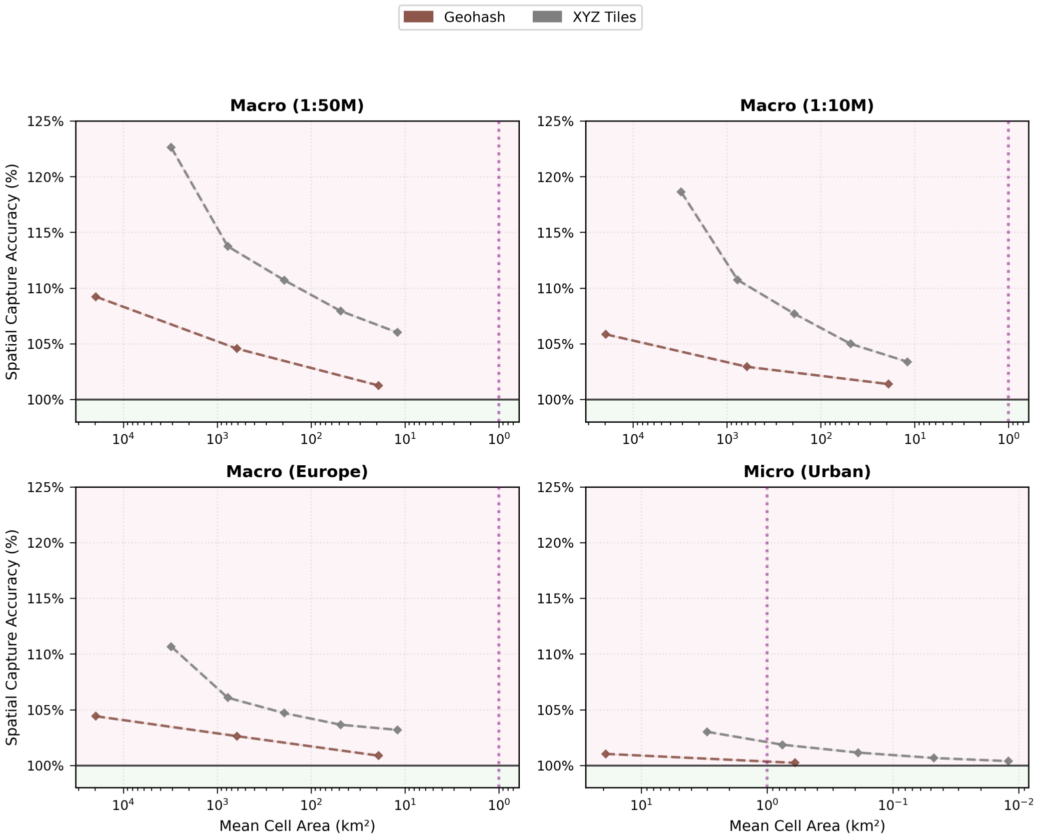

Fig. A5. Spatial Capture Accuracy of Planar Legacy Grids.

Table A3. Resolution step-back trade-off: break-even query count (N) at the peak-accuracy operating point and at up to three coarser resolution steps. Rows below 98% accuracy are shown for context only (*italic*). Canonical vector baselines: Macro = 4.40 s, Micro = 0.90 s.

Grid	Scale	Step	Res.	Area (km^2)	Acc. (%)	B-E (N)
H3	Macro (1:50m)	Peak	8	0.74	100.0	23
		−1	7	5.16	99.8	**3**
		−2	6	36.10	99.0	**1**
	Micro (Urban)	Peak	10	0.02	100.0	31
		−1	9	0.10	100.0	**5**
		−2	8	0.74	99.9	**1**
S2	Macro (1:50m)	Peak	12	1.23	99.9	209
		−1	11	4.95	99.9	**52**
		−2	10	19.80	98.8	**13**
	Micro (Urban)	Peak	16	<0.01	100.0	1,588
		−1	15	0.02	100.0	394
		−2	14	0.08	100.0	**96**
		−3	13	0.31	99.8	**24**
rHEALPix	Macro (1:50m)	Peak	8	1.44	99.9	3,560
		−1	7	12.94	99.6	395
	Micro (Urban)	Peak	9	0.16	99.9	3,673
		−1	8	1.44	99.7	410
ISEA4H	Macro (1:50m)	Peak	11	12.20	99.7	1,105
		−1	10	48.60	98.9	**275**
	Micro (Urban)	Peak	14	0.19	100.0	2,430
		−1	13	0.76	99.9	604
		−2	12	3.04	99.7	**152**
Geohash	Micro (Urban)	Peak	7	0.60	100.2	87
		−1	6	19.10	101.0	**3**

Bold = break-even below 100 queries at ≥98% accuracy.